Numerical investigation of atmospherelike flows in a spherical geometry

Vadim Travnikov and Christoph Egbers

Department of Aerodynamics and Fluid Mechanics, Brandenburg University of Technology Cottbus-Senftenberg,
Siemens-Halske-Ring 15a, D-03046, Cottbus, Germany

Buoyancy-driven convection flows play a crucial role in global heat and momentum transport in atmosphere. Simplified planetary and stellar atmospheres can be described by a spherical gap geometry with special boundary conditions for the temperature. In the spherical gap, the dielectrophoretic effect is used to synthesize the radial gravity field. Lateral thermal boundary conditions are used to model solar radiation at the equator and at the poles. The temperature reaches a maximum value at the equator and becomes colder near the poles. In the case of a rotating gap, the influence of the Coriolis and centrifugal forces are taken into account. Different regimes of the two-dimensional steady basic flow are discussed in dependence on the Taylor number and Rayleigh number and for the radii ratio $\eta = R_{in}/R_{out}$, where R_{in}, R_{out} are the radii of the inner and outer surfaces, respectively. Linear instability theory is used to study when the basic flow becomes unstable. The critical Rayleigh number at which the steady axisymmetric basic flow becomes time-dependently axisymmetric or three dimensional is found to be a function of the Taylor number. Furthermore, the critical azimuthal wave number m_c, which is responsible for the structure of the supercritical three-dimensional flow, and the critical frequency of the perturbation ω_c were found. The spatial location of the perturbation helps to understand the origin of the instability.

I. INTRODUCTION

Large-scale rotating flows play a fundamental role in atmospheric applications. In particular, the study of planetary atmospheres is of great importance for weather forecasting, climate, and the greenhouse effect. It is well known that atmospheric flows are caused by gravity, rotation of the planet, and heating due to solar radiation. This heating is inhomogeneous because the Sun's rays are perpendicular to the Earth's surface at the equator, causing the temperature to be higher than at the poles. To understand the dynamics of such flows, various simplified models have been proposed. A differentially heated, rotating cylindrical annulus is the most widely used geometry system to simulate atmospherelike flows. This configuration has been suggested by Hide [1] for investigating many effects that take place in the real atmosphere. Indeed, due to the heating of the outer surface and the cooling of the inner wall convective flow occurs because the temperature gradient is perpendicular to the Earth's gravity. Moreover, if the system rotates, then the Coriolis force leads to the inclination of the convective basic flow as in the real atmosphere. If the rotation rate increases, then the gradient of the temperature field is no longer parallel to the pressure gradient, caused baroclinic instability. The flow becomes three dimensional and takes the form of steady waves with different wave numbers in the azimuthal direction. This flow has been investigated very thoroughly by many authors experimentally [1–3]. Improvement of the computational possibilities and numerical methods led to publications in which numerical investigations of the various regimes and transitions [4–6] were carried out. They found quite good agreement with experiments. Hence, the combination of the most essential components of the at-

mospheric flow such as gravity, rotation, and heating causes the formation of large-scale circulation and the occurrence of baroclinic instability that can be made visible due to the appearance of the wave structure of the supercritical flow. The studies cited above were performed in the cylindrical annulus with horizontal endwalls, but the Coriolis force in the atmosphere depends on the polar angle. To take this effect into account, the design of the experiment has been changed by adding the conical geometry of the bottom and top walls. The experimental investigation of the flow with such sloping endwalls [7–10] is a useful tool to study the nonlinear effects and transition into the chaotic states in the atmosphere using the comparatively easy geometry.

Unfortunately, the annulus configuration has some restrictions. First, the convective basic flow is concentrated in the vicinity of the isothermal boundaries and causes a stable boundary layer. Second, solar radiation is responsible for the differential heating of the Earth's surface. This heating is particularly strong in the tropics. Air becomes lighter, rises, and moves toward the poles, where it becomes denser and sinks down. This circulation looks much more complex than in the classical annulus. Therefore, a new experiment has recently been performed in the cylindrical cavity [11,12]. Only part of the bottom boundary is heated (corresponding to the ground at the equator) and part of the upper boundary (corresponding to the pole), which is closer to the rotation axis, is cooled. The main result of this new atmospherelike experiment was that the coexistence of baroclinic and convective instabilities was detected.

Although many results have been obtained using the cylindrical geometry, the spherical geometry is most natural for the investigation of the atmospherelike flows. The atmosphere

TABLE I. List of constants for the Novec 7200.

Energy dissipation factor h_{diss}	5.525×10^{-2}
Volume expansion coefficient α (K^{-1})	1.605×10^{-3}
Coefficient of thermal permittivity γ (K^{-1})	2.407×10^{-3}
ac frequency f (Hz)	10^4
Permittivity ϵ_r	7.393
Density ρ (kg m^{-3})	1420
Spec. heat capacity C_p (J K^{-1} kg^{-1})	1220
Kinematic viscosity ν (m^2 s^{-1})	4.708×10^{-7}
Thermal diffusivity κ (m^2 s^{-1})	4.5139×10^{-8}

of the Earth has three cells: the Hadley cell, the polar cell, and the Ferrel cell between them. This structure occurs due to the differential heating and Earth's rotation and is crucial for understanding the flow dynamics. Moreover, we have new numerical tools and specific computer codes that have been developed using very exact spectral methods [13] that enable these investigations.

The presented work provides numerical support for the AtmoFlow experiment [14] on the International Space Station (ISS). This experiment is to follow the successful GeoFlow series [15–20], in which geophysically relevant convective flows were studied under microgravity conditions. Atmospherelike flows will be simulated on the ISS to eliminate the influence of Earth's gravity. The Novec 7200 fluid (Pr = 10.43) is used as a working fluid in this experiment (Table I).

The paper is structured as follows. We begin the formulation of the problem by discussing the geometry and special boundary conditions for the temperature in Sec. II A and explaining the buoyancy force in Sec. II B. After formulating the governing equations in Sec. II D, we present the numerical method in Sec. III. The classification of the basic flows for different Rayleigh numbers and Taylor numbers is discussed in Sec. IV A. The linear instability analysis is carried out in Sec. V.

II. FORMULATION OF THE PROBLEM

A. Geometry and boundary conditions for the temperature

The presented work deals with the numerical simulation of a simplified atmospherelike flow in the spherical gap be-

tween two spherical surfaces (Fig. 1, left), which is filled with dielectric fluid. The dielectrophoretic effect, discussed below, enables the creation of the radial force field. The radii ratio is $\eta = R_{\text{in}}/R_{\text{out}} = 0.7$ in the AtmoFlow experiment and $\eta = 0.7$, $\eta = 0.8$ for the numerical research. The real spherical gap, which is much narrower ($\eta = 0.997$), cannot be realized in the experiment because some space for technical devices is necessary. But this value cannot be used from the numerical point of view because in this case, an extremely large resolution in the polar and azimuthal directions would be required as we will see in Sec. III.

The next important issue is connected with the formulation of relevant thermal boundary conditions. Of course, realistic boundary conditions are extremely complex due to many factors such as radiative exchanges, ocean flows, or surface topography, but thermal boundary conditions should, nevertheless, obey the following features in three regions [14]: (1) the temperature at the equator reaches its maximum value because of infrared radiation, caused by solar heating; (2) the temperature sinks in the upper atmosphere of both poles; and (3) moderate temperature distribution between the polar and equatorial regions. The temperature on the inner surface can be simulated based on the relation

$$T_{\text{in}}(\theta) = \left(\frac{T_{\text{hot}} + T_{\text{cold}}}{2}\right) + \left(\frac{T_{\text{hot}} - T_{\text{cold}}}{2}\right) \sin^n \theta, \quad (1)$$

where the factor n controls the width of the distribution. When $n = 100$, the temperature decreases from T_{hot} at the equator to $(T_{\text{hot}} + T_{\text{cold}})/2$ within 30°. The temperature at the outer surface should be constant, but not at the poles, where large gradients in the polar direction have to be simulated. These gradients can be controlled by the thermal layer parameter a_{th}. The analytical expression on the outer surface can be suggested in the form

$$T_{\text{out}}(\theta) = T_{\text{cold}} + \left(\frac{T_{\text{hot}} - T_{\text{cold}}}{2}\right) \frac{\cosh(a_{\text{th}} \cos \theta) - \cosh(a_{\text{th}})}{1 - \cosh(a_{\text{th}})}, \quad (2)$$

where $a_{\text{th}} = 50$. This choice of parameter increases the temperature from T_{cold} on the poles to $(T_{\text{cold}} + T_{\text{hot}})/2$ within 30° according to the three-cell atmospheric model. Note that the tested functions Eqs. (1) and (2) obey all three above-mentioned conditions. These novel polar angle-dependent boundary conditions meet the real situation much better in
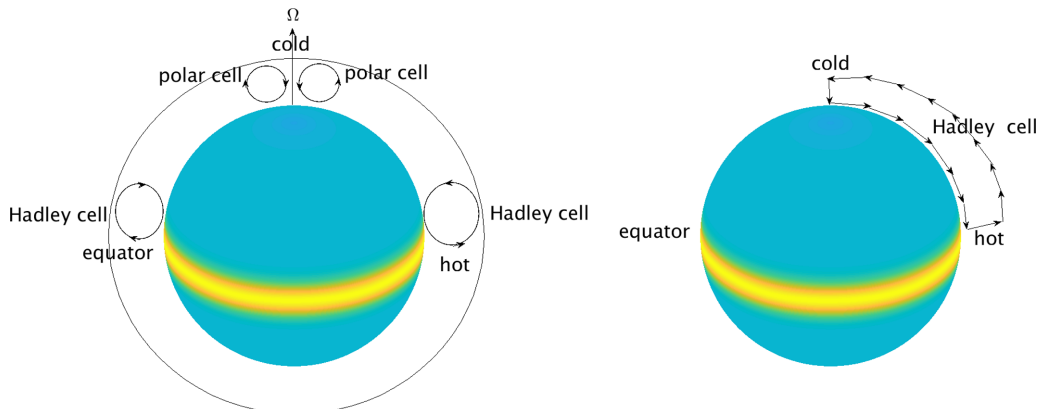

FIG. 1. Simplified global atmospheric circulation from (left) and one-cell model (right).
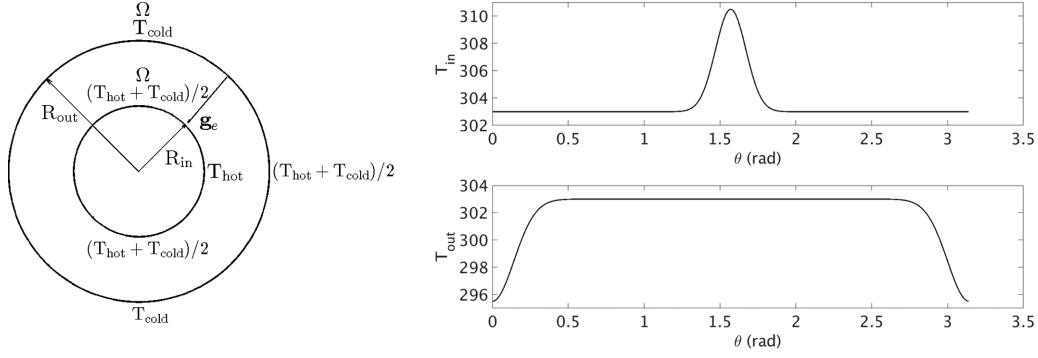
FIG. 2. The geometry of the problem (left), boundary conditions for the temperature (right).

contrast to the case when each surface is maintained at constant temperature. The geometry of the problem and temperature profiles on the inner and outer surfaces are shown by $T_{\text{cold}} = 295.5$ K and $T_{\text{hot}} = 310.5$ K in Fig. 2.

B. Derivation of the radial force field

To generate the radial force field, the electric field is imposed on a dielectrically incompressible fluid of density ρ and a temperature-dependent permittivity $\epsilon(T)$. The force density generated by the electric field $\mathbf{E}$ can be expressed according to [21]:

$$\mathbf{f}_e = \rho_e \mathbf{E} - \frac{1}{2}\mathbf{E}^2 \nabla \epsilon(T) + \nabla \left[\frac{1}{2}\rho \left(\frac{\partial \epsilon}{\partial \rho} \right)_T \mathbf{E}^2 \right], \quad (3)$$

where the first term is the density of the Coulomb force with a free charge ρ_e. The second term represents the dielectrophoretic force density, $\mathbf{f}_{\text{dep}}$. The third term corresponds to the electrostriction force and can be united with the pressure gradient. The Coulomb force is negligible if the frequency of the imposed electric field f is much higher than all frequencies responsible for the fluid behavior. These conditions can be expressed as follows: $f \gg \tau_e^{-1}, t_\nu^{-1}, t_\kappa^{-1}$, where $\tau_e = \epsilon_0 \epsilon_r / \sigma_e$ is the charge relaxation time (ϵ_0 is the vacuum permittivity, ϵ_r is the dielectric constant, and σ_e is the electrical conductivity), $t_\nu = d^2/\nu$ is the viscous relaxation time, $t_\kappa = d^2/\kappa$ is the thermal relaxation time (ν is the kinematic viscosity, κ is the thermal diffusivity), and $d = R_{\text{out}} - R_{\text{in}}$ is the width of the spherical gap. Furthermore, the width of the gap must be much larger than the thickness of the Debye layer on the electrodes, i.e., $d \gg \delta_D$ [22,23]. Since all of these conditions are met, only the dielectrophoretic force affects the flow and must be considered. The dielectrophoretic force can be rewritten based on the well-known relation

$$-\frac{1}{2}\mathbf{E}^2 \nabla \epsilon(T) = -\frac{1}{2}\nabla[\mathbf{E}^2 \epsilon(T)] + \frac{1}{2}\epsilon(T)\nabla \mathbf{E}^2. \quad (4)$$

The first term can be combined with the pressure, and the second term can be understood as the buoyancy force. However, instead of the temperature-dependent density, $\rho(T)$, we now have the temperature-dependent electric permittivity $\epsilon(T)$. Furthermore, the behavior of the electric permittivity can be approximated by a linear function of the temperature T:

$$\epsilon(T) = \epsilon_0 \epsilon_r [1 - \gamma(T - T_{\text{cold}})]. \quad (5)$$

We can interpret Eq. (5) as the "equation of state" that connects permittivity with the temperature (γ is the coefficient of thermal permittivity) similarly to the corresponding equation for the density that is widely used in many convective problems. To understand where the gravity field comes from, the force $\mathbf{f}_{\text{dep}}$ can be written after a little algebra as follows:

$$\mathbf{f}_{\text{dep}} = -\rho \gamma (T - T_{\text{cold}})\mathbf{g}_e, \quad \mathbf{g}_e = \frac{\epsilon_0 \epsilon_r}{2\rho} \nabla \mathbf{E}^2, \quad (6)$$

where $\mathbf{g}_e$ is the artificial gravity field induced by the electric field.

Now we emphasize an important difference between the problem under consideration and many other convective problems [e.g., in natural convection, Rayleigh-Bénard (RB) convection, etc.]. In RB convection, the gravity does not change, and the flow is controlled due to the temperature gradient, while in our case, $\Delta T = (T_{\text{hot}} - T_{\text{cold}})/2$ is maintained at a constant value ($\Delta T = 7.5\,K$), and the flow is triggered by varying the voltage or artificial gravity. We underline that the dielectrical effect is a very useful tool to simulate an artificial gravity under the microgravity conditions in planar [24,25], cylindrical [26], and spherical [16,19,27,28] geometries. The theoretical background and applications of this effect can be found in Ref. [29]. Note that the microgravity condition is particularly important because the Earth's gravity is at least 100 times stronger than artificial $\mathbf{g}_e$. Hence, to eliminate the effect of Earth's gravity, corresponding experiments must be performed in space, e.g., on the ISS.

C. Influence of dielectrical heating

As we showed in previous publications [14,20], because of the high frequency of the applied electric field, f, the volumetric heating must be taken into account in the energy equation by the source term according to the relation

$$H_E = \frac{2\pi f \epsilon_0 \epsilon_r h_{\text{diss}}}{\rho C_p} \mathbf{E}^2, \quad (7)$$

where h_{diss} is the energy dissipation factor and C_p is the specific heat capacity. Substituting all necessary values from Table I and taking into account the fact that the gap width in the AtmoFlow experiment is $d = 0.0081$ m and the voltage between two surfaces is $V_{\text{rms}} = 1000$ V (it is a variable value), we obtain $H_E \approx 0.2$ K/s. Note that we have electric-field-dependent (via the voltage) gravity $g_e \sim V_{\text{rms}}^2 r^{-5}$ in the

Navier-Stokes equation [27] and $H_E \sim V_{\text{rms}}^2 r^{-4}$ in the energy equation. Hence, the source term and the gravity are coupled parameters ($H_E \sim g_e$).

D. Equations

We consider an incompressible viscous dielectric fluid in the Boussinesq approximation in the spherical gap. In general form, the problem under consideration can be described by the Navier-Stokes equation for the velocity,

$$\frac{\partial \mathbf{U}}{\partial t} + (\mathbf{U} \cdot \nabla)\mathbf{U} = -\nabla p_{\text{eff}} - \gamma(T - T_{\text{cold}})\mathbf{g}_e + \nu\nabla^2\mathbf{U}$$
$$- 2\mathbf{\Omega} \times \mathbf{U} - \frac{\rho(T)}{\rho_0}\mathbf{\Omega} \times (\mathbf{\Omega} \times \mathbf{r}), \quad (8)$$

where $\mathbf{U}$ is the velocity field and t is the time,

$$p_{\text{eff}} = \frac{p}{\rho_0} - \frac{\gamma\epsilon_0\epsilon_r(T - T_{\text{cold}})E^2}{2\rho_0} - \frac{1}{2}\left(\frac{\partial\epsilon}{\partial\rho}\right)_T E^2, \quad (9)$$

$\rho_0 = \rho(T_{\text{cold}})$, $\mathbf{\Omega}$ is the rate of rotation, and the energy equation for the temperature

$$\frac{\partial T}{\partial t} + (\mathbf{U} \cdot \nabla)T = \kappa\nabla^2 T + H_E, \quad (10)$$

the continuity equation

$$\nabla \cdot \mathbf{U} = 0, \quad (11)$$

and the Gauss equation

$$\nabla \cdot [\epsilon(T)\nabla\upsilon] = 0, \quad (12)$$

where υ is the electric potential: $\mathbf{E} = -\nabla\upsilon$.

The equation for permittivity, Eq. (5), was substituted into the Navier-Stokes equation. In the term corresponding to the centrifugal force, the temperature-dependent density must be taken into account. Therefore, the equation of state

$$\rho(T) = \rho_0[1 - \alpha(T - T_{\text{cold}})], \quad (13)$$

where α is the volume expansion coefficient, $\rho_0 = \rho(T_{\text{cold}})$ is necessary to complete the system of equations.

Now let us formulate the boundary conditions for the velocity field. The first set (BC I) corresponds to the no penetration condition for U_r and no-slip for U_θ, U_ϕ,

$$U_r = 0, \quad U_\theta = 0, \quad U_\phi = 0, \quad (14)$$

on the inner bounding surface $r = R_{\text{in}}$ and on the outer bounding surface $r = R_{\text{out}}$. The second set (BC II) is [Eq. (14)] on the inner surface and no penetration condition for the radial velocity component and free-slip for U_θ, U_ϕ on the outer bounding surface,

$$U_r = 0, \quad \frac{\partial}{\partial r}\left(\frac{U_\theta}{r}\right) = 0, \quad \frac{\partial}{\partial r}\left(\frac{U_\phi}{r}\right) = 0. \quad (15)$$

The motivation for solving a problem with these constraints is as follows. While the first set, Eq. (14), is realized in the new AtmoFlow experiment to be performed on the International Space Station, the second set, Eq. (15), is closer to real atmospheric conditions. The boundary conditions for temperature and the electric potential are

$$T = T_{\text{in}}(\theta), \quad \upsilon = V_{\text{rms}}, \quad (16)$$

on the inner surface $r = R_{\text{in}}$,

$$T = T_{\text{out}}(\theta), \quad \upsilon = 0, \quad (17)$$

on the outer surface $r = R_{\text{out}}$. The time-dependent voltage $V(t) = V_0 \cos 2\pi f t$ was replaced by the root-mean-squared value $V_{\text{rms}} = \sqrt{\langle V^2(t)\rangle} = V_0/\sqrt{2}$ according to the time-averaged relationship over one period of the voltage variation $T_e = f^{-1}\langle V^2(t)\rangle = \frac{1}{T_e}\int_0^{T_e} V^2(t)dt$. Conditions for this replacement were numerically derived in Refs. [30,31] and can be briefly formulated as follows. First, the Prandtl number of the working fluid must be large (Pr $\gg$ 1). Furthermore, the frequency f must obey two conditions: $f \gg t_\nu^{-1}$ and $f \gg \tau_e^{-1}$. Considering $f = 10^4$ Hz, Pr $= 10.43$, $\nu = 4.708 \times 10^{-7}$ m^2 s^{-1}, $d = R_{\text{out}} - R_{\text{in}} = 0.0081$ m, we can conclude that all these conditions are fulfilled (Table I).

Introducing the dimensionless temperature T^* according to $T - T_{\text{cold}} = \Delta T T^*$, where $\Delta T = (T_{\text{hot}} - T_{\text{cold}})/2$, d for the length $r = r^* d$, κ/d for the velocity $U = U^*\kappa/d$, $t_\kappa = d^2/k$ for the time $t = t^* d^2/\kappa$, V_{rms}/d for the electric field $\mathbf{E} = \mathbf{E}^* V_{\text{rms}}/d$, $\rho_0\kappa^2/d^2$ for the pressure and $p = p^*\rho_0\kappa^2/d^2$, the governing equations can be expressed as follows (without asterisks):

$$\text{Pr}^{-1}\left[\frac{\partial\mathbf{U}}{\partial t} + (\mathbf{U} \cdot \nabla)\mathbf{U}\right]$$
$$= -\text{Pr}^{-1}\nabla p + \nabla^2\mathbf{U}$$
$$- \frac{1}{4}\text{Ra}_E \cdot T \cdot \nabla[\nabla\upsilon_0(r) + \nabla\upsilon_1(r,\theta,\phi)]^2$$
$$- \sqrt{\text{Ta}}\mathbf{e}_z \times \mathbf{U} + A \cdot \text{Tr}\sin\theta\mathbf{s}, \quad (18)$$

where $\mathbf{e}_z = \cos\theta\mathbf{e}_r - \sin\theta\mathbf{e}_\theta$, $\mathbf{s} = -(\sin\theta\mathbf{e}_r + \cos\theta\mathbf{e}_\theta)$ are unit vectors,

$$\frac{\partial T}{\partial t} + (\mathbf{U} \cdot \nabla)T = \nabla^2 T + \frac{\text{Ra}_E}{\text{Ra}_T}[\nabla\upsilon_0(r) + \nabla\upsilon_1(r,\theta,\phi)]^2, \quad (19)$$

$$\nabla^2\upsilon_1(r,\theta,\phi) = \frac{B}{1 - B \cdot T}\nabla T \cdot [\nabla\upsilon_0(r) + \nabla\upsilon_1(r,\theta,\phi)], \quad (20)$$

$$\text{Ra}_E = \frac{2\epsilon_0\epsilon_r\gamma}{\rho\nu\kappa}V_{\text{rms}}^2\Delta T, \quad (21)$$

is the Rayleigh number and

$$\text{Ta} = \left(\frac{2\Omega d^2}{\nu}\right)^2 \quad (22)$$

is the Taylor number. Further parameters are defined as $\text{Ra}_T = \frac{C_p\gamma\Delta T^2}{\pi\nu f h_{\text{diss}}}$, $B = \gamma\Delta T$, $A = \frac{1}{4}\alpha\Delta T\text{PrTa}$. The electric field $\mathbf{E}$ can be divided into two parts (θ is the polar angle and ϕ is the azimuth angle),

$$\mathbf{E} = \mathbf{E}_0(r) + \mathbf{E}_1(r,\theta,\phi), \quad (23)$$

$$\mathbf{E}_0(r) = -\nabla\upsilon_0(r), \quad (24)$$

$$\mathbf{E}_1(r,\theta,\phi) = -\nabla\upsilon_1(r,\theta,\phi). \quad (25)$$

TABLE II. List of dimensionless parameters ($\Delta T = 7.5$ K).

Rayleigh number, Ra_E	$2\epsilon_0\epsilon_r\gamma\Delta T V_{\mathrm{rms}}^2/(\rho\nu\kappa)$	$0\text{–}2.45\times10^5$
Taylor number, Ta	$(2\Omega d^2/\nu)^2$	$0\text{–}4\times10^5$
Prandtl number, Pr	ν/κ	10.43
Radii ratio, η	R_1/R_2	0.7, 0.75, 0.8
A	$\alpha\Delta T\mathrm{Pr}\mathrm{Ta}/4$	$0\text{–}12555$
B	$\gamma\Delta T$	0.01805
Ra_T	$C_p\gamma\Delta T^2/(\pi\nu f h_{\mathrm{diss}})$	202134

Meanwhile, the field $\mathbf{E}_0(r)$, satisfying the expression $\nabla \cdot \mathbf{E}_0(r) = 0$, can be calculated analytically

$$\mathbf{E}_0(r) = \frac{\eta}{(1-\eta)^2}\frac{1}{r^2}\mathbf{e}_r. \tag{26}$$

The field $\mathbf{E}_1(r,\theta,\phi)$ has a more complex form since it generally depends on all three coordinates and must be found numerically by solving Eq. (20). Substituting $\mathbf{E}_0(r)$ in Eq. (6), we obtain the well-known r^{-5} dependence [27]. It is clear that the second field occurs due to the temperature-dependent function $\epsilon(T)$. The boundary conditions for the temperature T and the electric potential υ_1 are

$$T_{\mathrm{in}}(\theta) = 1 + \sin^n\theta, \quad \upsilon_1 = 0, \tag{27}$$

on the $r_{\mathrm{in}} = R_{\mathrm{in}}/d = \eta/(1-\eta)$ and

$$T_{\mathrm{out}}(\theta) = \frac{\cosh(a_{\mathrm{th}}\cos\theta) - \cosh(a_{\mathrm{th}})}{1 - \cosh(a_{\mathrm{th}})}, \quad \upsilon_1 = 0, \tag{28}$$

on the $r_{\mathrm{out}} = R_{\mathrm{out}}/d = 1/(1-\eta)$. The parameters Ra_T and B do not change with fixed ΔT. Parameter A depends only on the Taylor number (for a fixed Prandtl number). Therefore, we can study a convective flow that depends on the Rayleigh number (or voltage V_{rms}) and the Taylor number (or rotation rate Ω).

Finally, let us appreciate the influence of the dimensionless parameters Ra_T, B, and A in more detail. The values of these parameters for $\Delta T = 7.5$ K are $\mathrm{Ra}_T = 202134$, $B = 0.01805$, and $A = 0.03139\mathrm{Ta}$. Note that even for moderate Rayleigh numbers, e.g., $\mathrm{Ra}_E = 5\times10^4$, the influence of the dielectrical heating, expressed in terms of $\mathrm{Ra}_E/\mathrm{Ra}_T \approx 0.25$, is essential and must be taken into account. This relation increases drastically as Ra_E increases, particularly in the nonrotating and slowly rotating cases. Parameter A is responsible for the influence of the centrifugal force that will be discussed later in Sec. V D. The list of dimensionless parameters can be found in Table II.

III. NUMERICAL METHOD

The fully three-dimensional pseudospectral numerical code for the spherical geometry was developed by R. Hollerbach [13]. The poloidal-toroidal representation of the velocity field

$$\mathbf{U} = \nabla\times\nabla\times(\Phi\mathbf{e}_r) + \nabla\times(\Psi\mathbf{e}_r) \tag{29}$$

has many advantages. First, the velocity field automatically obeys the continuity equation. The second reason is that the separate equations for poloidal Φ and toroidal Ψ potentials are obtained by applying the operators $\nabla\times\nabla\times$ and $\nabla\times$,

respectively. Note that they are coupled due only to the nonlinear term in the Navier-Stokes equation. Moreover, applying the above operators eliminates pressure. After performing the mapping $r(z) = \frac{1}{2}[z + \frac{1+\eta}{1-\eta}]$, where $z \in [-1,+1]$, any scalar function can be expanded in terms of the Chebyshev polynomials in the radial direction and in terms of spherical harmonics in the polar and azimuthal directions according to

$$\Phi(t,r(z),\theta,\phi) = \sum_{m=0}^{MU}\sum_{\ell=\ell'}^{LU}\sum_{k=1}^{KU+4}[g_{ck\ell m}(t)\cos(m\phi)$$
$$+ g_{sk\ell m}(t)\sin(m\phi)]T_{k-1}(z)P_\ell^m(\cos\theta)$$

$$\Psi(t,r(z),\theta,\phi) = \sum_{m=0}^{MU}\sum_{\ell=\ell'}^{LU}\sum_{k=1}^{KU+2}[f_{ck\ell m}(t)\cos(m\phi)$$
$$+ f_{sk\ell m}(t)\sin(m\phi)]T_{k-1}(z)P_\ell^m(\cos\theta), \tag{30}$$

$\ell' = \max(1,m)$. Four boundary conditions are necessary for the poloidal potential and two for the toroidal potential. From Eq. (14) we obtain

$$\Phi = 0 \tag{31}$$

on both boundaries. This relation is equivalent to the no-penetration condition. The next two boundary conditions can be derived using the continuity equation. In the case of the no-slip boundary conditions Eq. (14) yields

$$\frac{\partial\Phi}{\partial r} = 0, \quad \Psi = 0, \tag{32}$$

on both surfaces. The free-slip boundary conditions become the following form:

$$\left(\frac{\partial^2}{\partial r^2} - \frac{2}{r}\frac{\partial}{\partial r}\right)\Phi = 0, \quad \left(\frac{\partial}{\partial r} - \frac{2}{r}\right)\Psi = 0. \tag{33}$$

A similar expressions apply to the temperature and electric potential:

$$T(t,r(z),\theta,\phi) = \sum_{m=0}^{MT}\sum_{\ell=m}^{LT}\sum_{k=1}^{KT+2}[t_{ck\ell m}(t)\cos(m\phi)$$
$$+ t_{sk\ell m}(t)\sin(m\phi)]T_{k-1}(z)P_\ell^m(\cos\theta)$$

$$\upsilon_1(t,r(z),\theta,\phi) = \sum_{m=0}^{MP}\sum_{\ell=m}^{LP}\sum_{k=1}^{KP+2}[p_{ck\ell m}(t)\cos(m\phi)$$
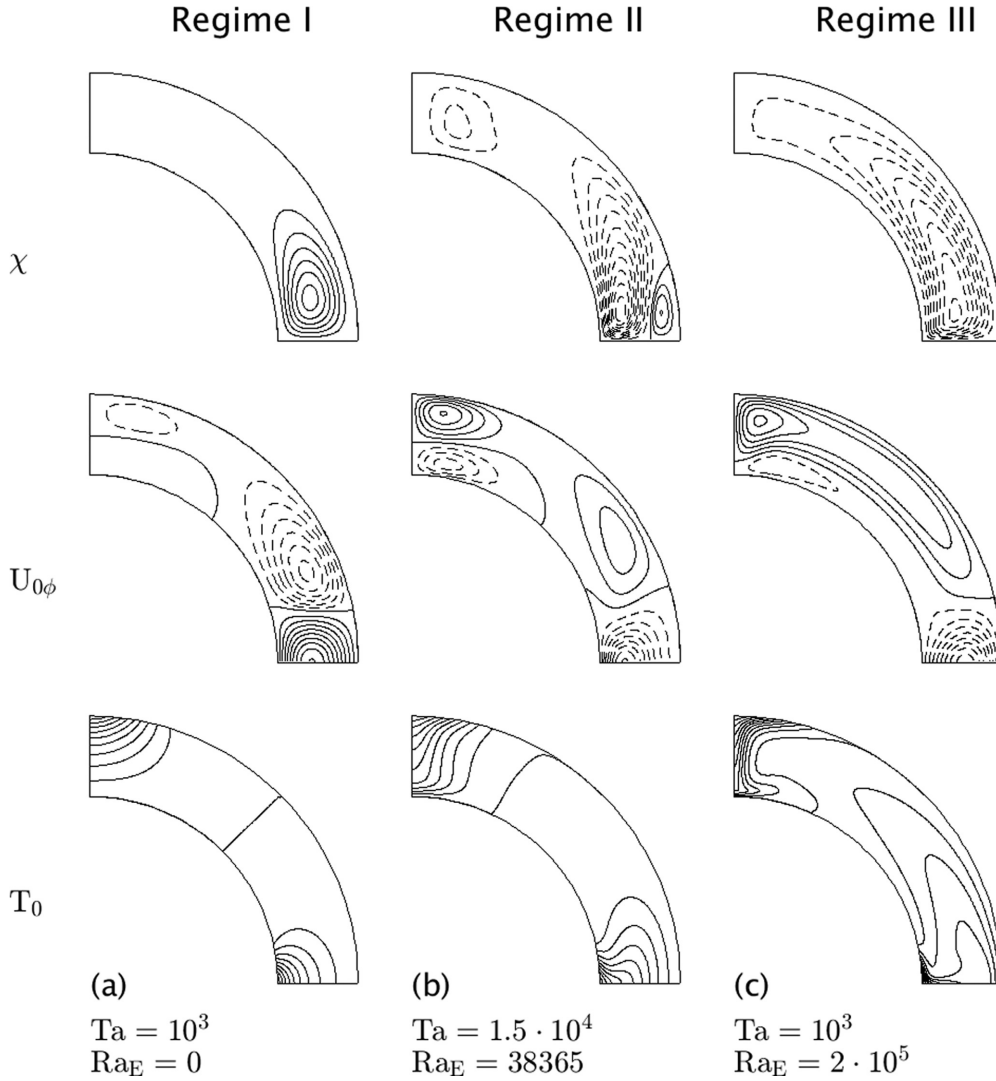$$+ p_{sk\ell m}(t)\sin(m\phi)]T_{k-1}(z)P_\ell^m(\cos\theta). \tag{34}$$

FIG. 3. Basic flow for $\eta = 0.7$ (BC I). The first row shows the contours of the meridional circulation χ with (a) $\chi_{\max} = 0.09$ (0.015); (b) $\chi_{\max} = 0.6$ (0.2), $\chi_{\min} = -6.0$ (0.6); and (c) $\chi_{\min} = -40.0$ (5.0). The dotted (solid) lines indicate a negative (positive) values of the stream function. The corresponding vortices rotate counterclockwise (clockwise). The second row shows the contours of the azimuthal velocity $U_{0\phi}$ with maximal and minimal values (a) $+0.18$ (0.02), -0.06 (0.01); (b) $+20.0$ (4.0), -40.0 (5.0); and (c) $+50.0$ (5.0), -80.0 (10.0). The contour intervals are shown in brackets. The third row shows the contours of the base temperature. The maximum value is $T_{\max} = 2.0$ at the equator, and the minimum value is $T_{\min} = 0.0$ on the outer surface at $\theta = 0$. The contour interval is 0.1.

The expressions for the poloidal and toroidal potentials reduce for the base axisymmetric flow ($m = 0$) as follows:

$$\Phi_0(t, r(z), \theta) = \sum_{\ell=1}^{LU} g_{0\ell}(t, r(z)) P_\ell(\cos\theta)$$

$$= \sum_{\ell=1}^{LU} \sum_{k=1}^{KU+4} g_{0k\ell}(t) T_{k-1}(z) P_\ell(\cos\theta)$$

$$\Psi_0(t, r(z), \theta) = \sum_{\ell=1}^{LU} f_{0\ell}(t, r(z)) P_\ell(\cos\theta)$$

$$= \sum_{\ell=1}^{LU} \sum_{k=1}^{KU+2} f_{0k\ell}(t) T_{k-1}(z) P_\ell(\cos\theta). \quad (35)$$

Similar expressions apply to the base temperature $T_0(t, r, \theta)$ and the base electric potential $\upsilon_1(t, r, \theta)$.

Twenty Chebyshev polynomials (KU = 20) were necessary to solve the problem in the radial direction for the velocity. The maximum value for the KT for the temperature is KT = 30. Unfortunately, many more Legendre polynomials were needed to obtain a grid-independent solution. While LU for the velocity field varies between LU = 80 and LU = 160, the LT should be at least LT = 100 due to boundary condition Eq. (1). The maximum value was LT = 240 to resolve the thermal boundary layer for a large Rayleigh number. To get, for example, a solution for $\eta = 0.7$, $Ra_E = 38000$, and $Ta = 10^4$ [Regime II, Fig. 3(b)] we need KU = KT = 20, LU = 80, and LT = 100, i.e., above these parameters the minimum value of the stream function $\chi_{\min} = -7.7248$ does not change.

Spectral coefficients were calculated using the predictor-corrector method. To obtain a steady two-dimensional basic flow, a time step Δt changes between $\Delta t = 10^{-3}$ and $\Delta t = 2 \times 10^{-5}$ for large Rayleigh numbers. The time step $\Delta t = 10^{-4}$ provides an excellent accuracy (within 0.03%) for stability analysis. However, for large Rayleigh numbers Δt should be reduced to $\Delta t = 10^{-5}$.

Note that both test functions Eqs. (27) and (28) not only satisfy all the required physical conditions but are also favorable from a numerical point of view. In other words, they can be represented in the form of a series with rapid convergence.

IV. BASIC FLOW

A. Flow patterns

The basic flow is steady, axisymmetric ($\frac{\partial}{\partial \phi} = 0$). Therefore, the meridional circulation can be expressed in terms of the stream function χ associated with the velocity components according to

$$U_{0r}(r, \theta) = \frac{1}{r^2 \sin \theta} \frac{\partial \chi}{\partial \theta}, \quad U_{0\theta}(r, \theta) = -\frac{1}{r \sin \theta} \frac{\partial \chi}{\partial r}. \quad (36)$$

The relationship between the stream function and the poloidal potential is

$$\chi(r, \theta) = -\sin \theta \frac{\partial \Phi_0(r, \theta)}{\partial \theta}. \quad (37)$$

Furthermore, we present the azimuthal velocity component $U_{0\phi}(r, \theta)$ and the base temperature $T_0(r, \theta)$. If the radii ratio η, the Prandtl number, and ΔT are fixed, then the flow depends on two control parameters: the Rayleigh number Ra_E and the Taylor number Ta. Depending on the point on the plane (Ta, Ra_E), this results in different basic flow patterns. The classification of such states for both kinds of the boundary conditions for the velocity is presented in the next sections.

1. Conductive state

When $\mathrm{Ra}_E = 0$ (no gravity) and Ta $= 0$ (no rotation), there is no flow [$U_0(r, \theta) = 0$]. However, the temperature, $T_{\mathrm{cond}}(r, \theta)$, corresponding to the conductive state can be found analytically (cf. Appendix).

2. Solutions for two rigid boundaries

In the case when no voltage is applied, i.e., $\mathrm{Ra}_E = 0$ but the spherical system rotates Ta > 0, the centrifugal force is responsible for the formation of the basic flow. The latter is predominantly located at the equator and the meridional vortex rotates clockwise [Fig. 3(a), Regime I, first row]. This structure is also preserved for large Taylor numbers and small Rayleigh numbers. The Coriolis force, $-2\rho_0 \Omega \times \mathbf{U}$, is responsible for the creation of the azimuthal component of the basic flow [Fig. 3(a), Regime I, second row]. Indeed, the radial component has the largest (negative) value at the equator. Therefore, the Coriolis force causes the positive azimuthal flow at and in the vicinity of the equator. For the same reason, the azimuthal velocity becomes negative if the fluid moves toward to the outer surface. The base temperature [Fig. 3(a), Regime I, third row] looks similar to the conductive state temperature. Indeed, the source term in the energy equation

does not affect the heat transfer and the convective term is small because the flow occurs only due to the centrifugal effects.

As the Rayleigh number increases, the buoyancy force becomes more and more important and leads to the new basic flow structure. Because the influence of the centrifugal force becomes smaller if the Taylor number decreases, the clockwise rotating vortex disappears and the meridional basic flow consists mainly of two parts. The first part occurs due to the buoyancy force and is located near the equator (*equatorial cell*) [Fig. 3(b), Regime II, first row]. The origin of this flow can be explained as follows. The boundary condition for the temperature at the inner surface creates a strong temperature gradient that has both radial and polar components. On the other hand, the gravity $\mathbf{g}_e$ has a radial direction. Therefore, this situation can be compared to natural convection when gravity and the temperature gradient are not parallel. This combination causes the convective flow. Due to equatorial heating, the density decreases and the fluid rises toward the outer surface. As the fluid moves poleward, it cools, the density increases, and the fluid descends toward the inner surface. Because the fluid is heavier than at the equator, the fluid travels down along the surface, closing the loop. Hence, the occurrence of the equatorial cell can be compared with the origin of the Hadley cell, that appears due to solar radiation at the equator. The poleward flow deviates toward the east due to the Coriolis force in the upper part of the vortex. In the vicinity of the inner surface, the flow deviates toward the west. The corresponding azimuthal component of the velocity is presented in Fig. 3(b), Regime II, second row. Hence, the equatorial or Hadley cell is inclined from the east to the west and causes an easterly wind in the north hemisphere, i.e., our numerical model is qualitatively in good accordance with three-cell atmospheric model. There is also a vortex at the pole (*polar cell*). This vortex is caused by convective motion of the fluid. Although the fluid in the vicinity of the pole is colder in contrast to the equatorial fluid it is still able to trigger the convection. First, the fluid rises toward the outer surface and moves toward the pole, where it becomes colder, denser, and descends toward the inner surface. Due to the high pressure at the pole, the fluid moves along the inner surface, completing the convective loop. The Coriolis force is again responsible for the inclination of the polar cell. The mechanism of this deviation is same as in the case of the equatorial cell. The corresponding flows are called polar winds. They move from northeast to southwest in the vicinity of the north pole and from southeast to northwest in the vicinity of the south pole. The polar cell is much weaker in contrast to the Hadley cell. This fact is also in accordance with the atmospheric three-cellular model. Unfortunately, not enough energy is produced to trigger the midlatitude or Ferrel cell in the case of $\eta = 0.7$ and no-slip boundary conditions. The base temperature undergoes a significant changes, as shown in Fig. 3(b), Regime II, third row. The temperature becomes a mushroom shape at the equator and strong radial gradients caused by convection.

When the Rayleigh number is large, at $\mathrm{Ra}_E = O(10^5)$, and the Taylor number is small, at Ta $= \mathrm{O}(10^3)$, the convective flow is propagated from the equator to the poles, as shown in Fig. 3(c), Regime III, first row. A meridional vortex rotates counterclockwise. This vortex occurs in the nonrotating or
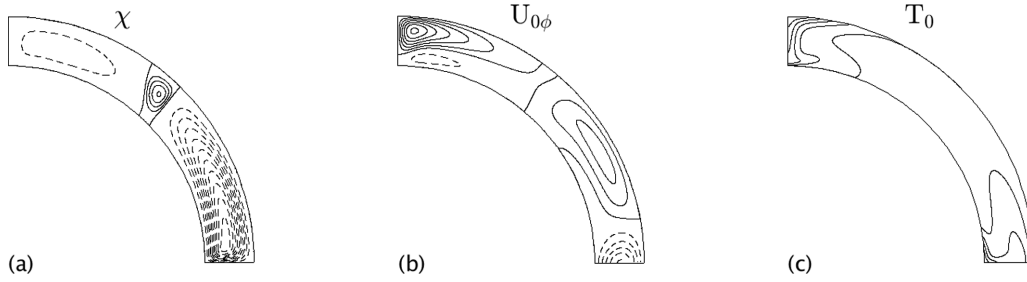
FIG. 4. Basic flow (Regime IV, BC I) for $\eta = 0.8$, $\text{Ta} = 2 \times 10^3$, and $\text{Ra}_E = 2 \times 10^5$. (a) Contours of the meridional circulation χ: $\chi_{\max} = 1.6 \, (0.4)$ and $\chi_{\min} = -50.0 \, (5.0)$. The dotted (solid) lines indicate a negative (positive) values of the stream function. The corresponding vortices rotate counterclockwise (clockwise). (b) Contours of the azimuthal velocity component $U_{0\phi}(r, \theta)$: $U_{0\phi\max} = 60.0 \, (10.0)$ and $U_{0\phi\min} = -100.0 \, (20.0)$. The dotted (solid) lines indicate a negative (positive) values of the azimuthal velocity. The contour intervals are shown in brackets. (c) The base temperature $T_0(r, \theta)$ with a contour interval of 0.2. The maximum value is $T_{\max} = 2.0$ at the equator, and the minimum value is $T_{\min} = 0.0$ on the outer surface at $\theta = 0$.

slowly rotating case and is a huge Hadley cell in accordance with the one-cell model (Fig. 1, right).

Physical features of the Regime III reflect in the numerical details. The polar gradients of the temperature [Fig. 3(c), Regime III, third row], $\partial T_0(r, \theta)/\partial \theta$, are due to the specific boundary conditions much larger than the similar gradients of the velocity. This explains why more Legendre polynomials are needed to resolve the thermal layer (LT = 240) in contrast to the LU = 160. Thickness of the thermal boundary layer in vicinity of the equator and poles is smaller in contrast the thickness of the boundary layer for the velocity ($\delta_{\text{th}} \ll \delta_u$). Therefore, more Chebyshev polynomials (KT = 30) are necessary to resolve thermal boundary layer than for the velocity KU = 20. Note that these features of the boundary layers are typical for fluids with large Prandtl numbers, i.e., as our working fluid with Pr = 10.43.

An additional pattern of the basic flow occurs in the narrow gap with $\eta = 0.8$ (Fig. 4). This new vortex is called the midlatitude or the Ferrel vortex, which is weaker than polar and Hadley cells because of absence of proper heat sources. Therefore the existence of Ferrel vortex fully depends on how strong polar and equatorial cells are. Note that the size of the polar cell is much larger than in the case presented in Fig. 3(b).

3. Solutions for the inner rigid and outer free boundary

The case, when the outer surface is free, is interesting from the point of view of physics because this constellation is slightly more consistent with the real atmospheric model. The corresponding numerical simulations of the basic flow are presented in Figs. 5 and 6.

The meridional circulation, corresponding to the Regime I [Figs. 5(a), first row] is the same as in the case with both rigid surfaces. The clockwise rotating vortex is caused by the centrifugal force, which is dominant if the buoyancy force is absent or small.

The Regime II [Fig. 5(b), first row] undergoes a remarkable transformation and differs from the corresponding regime considered in the previous section. Indeed, now the basic flow has not only polar and equatorial cells but also a clockwise rotating midlatitude or Ferrel cell between them. The other feature of this regime is that each of these cells occupies approximately 30% of the space from pole to equator. This is in

very good accordance with the three-cell atmospheric model. Because the outer bounding surface is free the azimuthal flow undergoes, of course, a significant change. The isolines of the azimuthal velocity at least at the vicinity of the outer surface are not the loops now. The maximum of the azimuthal component shifts toward the pole [Figs. 5(b), second row]. It is noteworthy that the azimuthal velocity component is positive in the vicinity of the equator and negative in other parts of the gap in Regime I [Figs. 5(a), second row] due to the Coriolis force as in the case considered above. If the Rayleigh number increases, then $U_{0\phi}$ changes their sign in the above regions [Figs. 5(b), second row]. Hence, we again obtain the correct direction of the Trade Winds using a very simple atmospheric model.

The meridional circulation [Fig. 5(c), Regime III, first row] has the similar shape as in the case with both rigid surfaces. The counterclockwise rotating vortex occupies the whole gap. Note that due to strong radial velocity component at the equator and polar velocity component in the vicinity of the poles the Coriolis force is very large even when the Taylor number is small. This leads to the formation of the large gradients of the azimuthal velocity components [Fig. 5(c), second row], which is important for understanding of the flow instability in the next section.

Furthermore, as in the case with two rigid surfaces, we have a pattern with one clockwise rotating small-scale vortex between two counterclockwise rotating vortices when the radii ratio increases, as presented in Fig. 6. This is a Ferrel vortex, which occurs because it obtains enough energy from the polar and Hadley cells.

Summarizing insights in form of the four regimes, gained from numerical investigation, we can now classify two-dimensional basic flows that have been obtained using the new thermal boundary conditions in the spherical gaps with $\eta = 0.7$ and $\eta = 0.8$. Of course, new flow patterns can occur if the gap becomes narrower, but these cases are out of the scope of this research.

We complete the presentation of the basic flow with a discussion of the influence of the additional electric field $\mathbf{E}_1(\mathrm{r}, \theta) = -\nabla \upsilon_1(\mathrm{r}, \theta)$. It is obvious that the radial component of the buoyancy force makes a considerable contribution to the convective flow. Indeed, working out this component, we can see that two terms are particularly important.
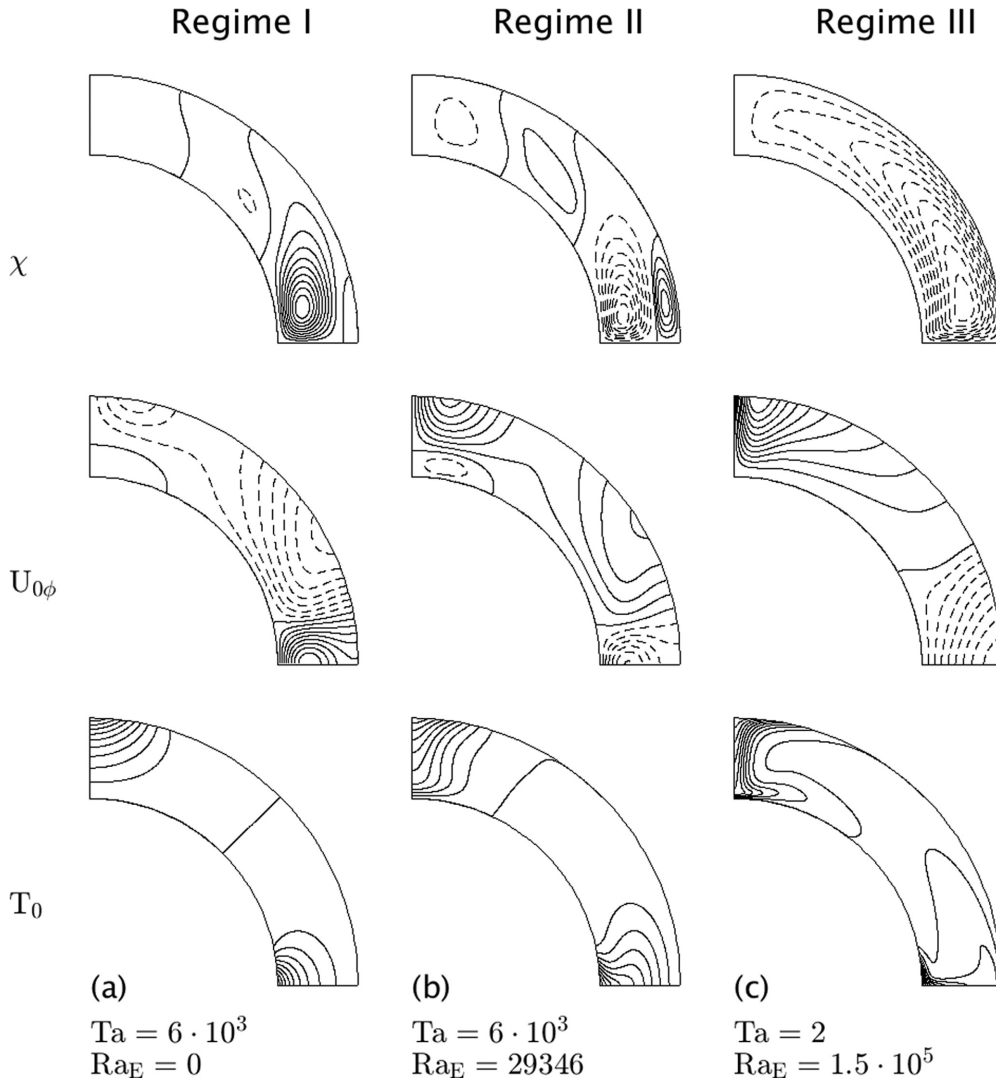
FIG. 5. Basic flow for $\eta = 0.7$ (BC II). The first row shows the contours of the meridional circulation χ with (a) $\chi_{max} = 0.18$ (0.02); (b) $\chi_{max} = 0.8$ (0.2), $\chi_{min} = -6.4$ (0.8); and (c) $\chi_{min} = -54.0$ (6.0). The dotted (solid) lines indicate a negative (positive) values of the stream function. The corresponding vortices rotate counterclockwise (clockwise). The second row shows the contours of the azimuthal velocity $U_{0\phi}$ with maximal and minimal values (a) $+0.8$ (0.1), -0.7 (0.1); (b) $+35.0$ (5.0), -30.0 (5.0); and (c) $+60.0$ (6.0), -8.0 (1.0). The contour intervals are shown in brackets. The third row shows the contours of the base temperature with a contour interval of 0.1. The maximum value is $T_{max} = 2.0$ at the equator, and the minimum value is $T_{min} = 0.0$ at the outer surface at $\theta = 0$.
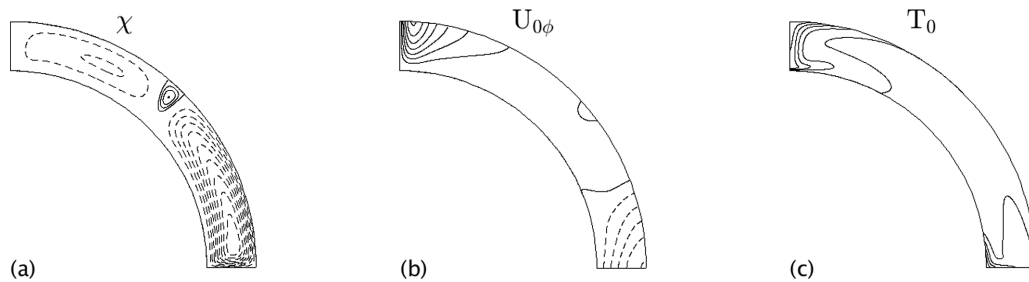
FIG. 6. Basic flow (Regime IV, BC II) for $\eta = 0.8$, Ta $= 10$, Ra$_E = 211770$. (a) Contours of the meridional circulation χ: $\chi_{max} = 3.0$ (1.0) and $\chi_{min} = -90.0$ (10.0). The dotted (solid) lines indicate negative (positive) values of the stream function. The corresponding vortices rotate counterclockwise (clockwise). (b) Contours of the azimuthal velocity component $U_{0\phi}(r, \theta)$: $U_{0\phi max} = 140.0$ (20.0) and $U_{0\phi min} = -20.0$ (4.0). The dotted (solid) lines indicate negative (positive) values of the azimuthal velocity. The contour intervals are shown in brackets. (c) The base temperature $T_0(r, \theta)$ with a contour interval of 0.2. The maximum value is $T_{max} = 2.0$ at the equator, and the minimum value is $T_{min} = 0.0$ on the outer surface at $\theta = 0$.
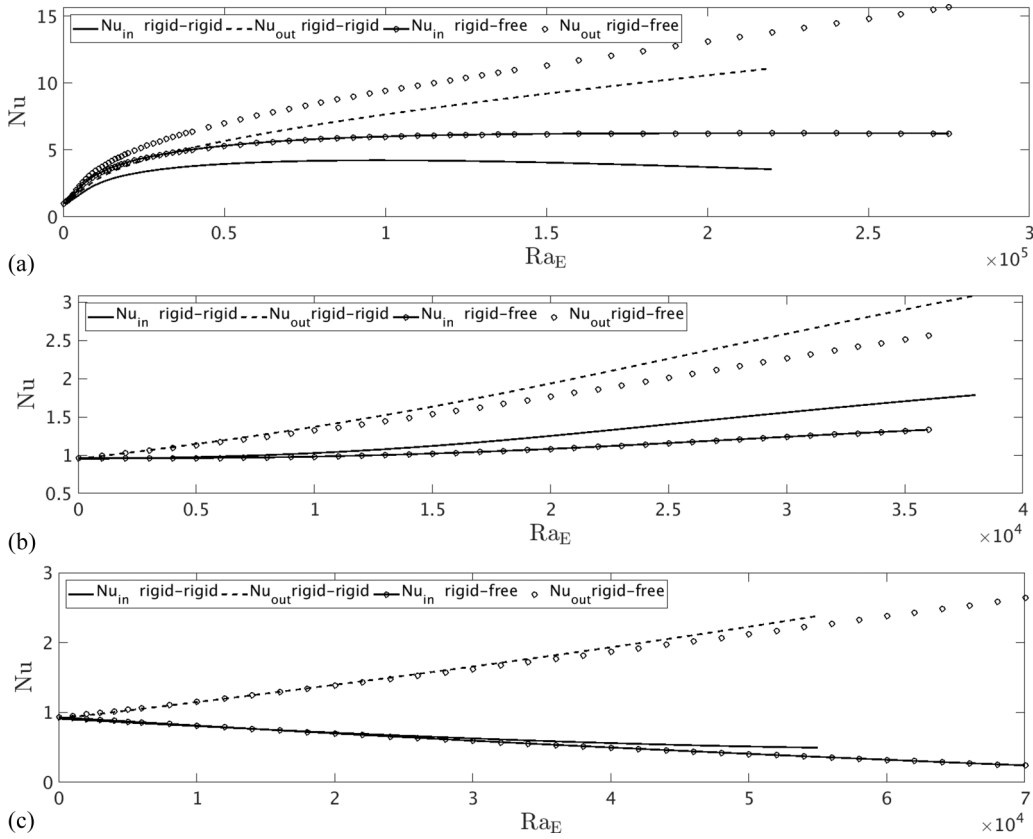
FIG. 7. Nusselt number for $\eta = 0.7$, (a) Ta = 0, (b) Ta = 15 000, and (c) Ta = 10^5.

The first is

$$F_{r1} = \mathrm{Ra}_E \frac{\eta^2}{(1-\eta)^4} \frac{T_0(r,\theta)}{r^5}, \tag{38}$$

which comes from the potential $\upsilon_0(r)$, which plays a highly essential role and the second is

$$F_{r2} = \mathrm{Ra}_E \frac{\eta}{2(1-\eta)^2} \frac{T_0(r,\theta)}{r^2} \frac{\partial^2 \upsilon_1(r,\theta)}{\partial r^2}, \tag{39}$$

which is a combination of the imposed electrical field $\mathbf{E}_0(\mathrm{r})$ and the additional field $\mathbf{E}_1$, caused by the temperature gradient in the Gauss equation. According to numerical simulations, the maximum value of the additional field is found on the inner surface at $\theta = \pi/2$ and is 100 times weaker than the imposed field $\mathbf{E}_0(\mathrm{r})$. Nevertheless, due to the second derivative, the relationship between the two terms is $F_{r2}/F_{r1} \approx 8\%$ at $(r,\theta) = [\eta/(1-\eta)], \pi/2), \eta = 0.7, \mathrm{Ra}_E = 38365$, and Ta = 7×10^3 for *both* kinds of the boundary conditions. Therefore, it is better to incorporate an additional field into the model under consideration.

B. Heat transfer

Heat transfer was studied in terms of the Nusselt number defined as

$$\mathrm{Nu}_{\mathrm{in}} = \frac{Q_{\mathrm{in}}^{\mathrm{conv}}}{Q_{\mathrm{in}}^{\mathrm{cond}}}, \quad \mathrm{Nu}_{\mathrm{out}} = \frac{Q_{\mathrm{out}}^{\mathrm{conv}}}{Q_{\mathrm{out}}^{\mathrm{cond}}}, \tag{40}$$

where

$$Q_{\mathrm{in}}^{\mathrm{conv}} = -\int_{S_{\mathrm{in}}} \frac{\partial T_0(r,\theta)}{\partial r} dS_{\mathrm{in}},$$

$$Q_{\mathrm{out}}^{\mathrm{conv}} = -\int_{S_{\mathrm{out}}} \frac{\partial T_0(r,\theta)}{\partial r} dS_{\mathrm{out}},$$

$$Q_{\mathrm{in}}^{\mathrm{cond}} = -\int_{S_{\mathrm{in}}} \frac{\partial T_{\mathrm{cond}}(r,\theta)}{\partial r} dS_{\mathrm{in}},$$

$$Q_{\mathrm{out}}^{\mathrm{cond}} = -\int_{S_{\mathrm{out}}} \frac{\partial T_{\mathrm{cond}}(r,\theta)}{\partial r} dS_{\mathrm{out}} \tag{41}$$

and $dS_{\mathrm{in,out}} = r_{\mathrm{in,out}}^2 \sin\theta d\theta d\phi$ for two types of the boundary conditions and radii ratios $\eta = 0.7$ and $\eta = 0.8$. According to the numerical calculations, the energy balance equation for all the cases considered is

$$\mathrm{Nu}_{\mathrm{in}} + \frac{\mathrm{Ra}_E}{\mathrm{Ra}_T} \frac{Q_E}{Q_{\mathrm{out}}^{\mathrm{cond}}} - \mathrm{Nu}_{\mathrm{out}} = 0, \tag{42}$$

where $Q_E = \int_V E^2 dV$, i.e., energy flux due to conduction through the inner surface together with the energy generated by the internal heating leaves the domain considered through the outer surface (Fig. 7). Despite the latitudinal dependence of the boundary conditions, the temperature corresponding to the purely conductive state can be calculated analytically. The solution can be found in the form of a series and is shown in the Appendix. The energy flux is

$$Q_{\mathrm{in}}^{\mathrm{cond}} = Q_{\mathrm{out}}^{\mathrm{cond}} = 0.1444 \frac{4\pi\eta}{(1-\eta)^2}. \tag{43}$$

Moreover, because the influence of the additional electric field υ_1 and $\frac{\partial \upsilon_1}{\partial r}$ is small, the Q_E can be calculated analytically. After a little algebra we have

$$Q_E = \frac{4\pi\eta}{(1-\eta)^2}. \tag{44}$$

Hence, taking into account Eq. (43), we can conclude that Q_E/Q^{cond} does not depend on the radii ratio η, and the energy balance equation can be written as

$$\text{Nu}_{\text{in}} + 6.93\frac{\text{Ra}_E}{\text{Ra}_T} - \text{Nu}_{\text{out}} = 0. \tag{45}$$

The following consequences can be drawn from the Eq. (45) and numerical calculations. (1) The influence of the dielectrical heating is $\sim\text{Ra}_E$. This feature of the model under consideration is very specific and differs from other models in which sources in the energy equations are negligible. (2) The heat transfer at Ta = 0, i.e., in the nonrotating case [Fig. 7(a)] is much stronger in contrast to the rotating case [Figs. 7(b) and 7(c)]. Hence, the rotation reduces the heat transfer. (3) The boundary conditions for the velocity affect the heat transfer at Ta = 0: The free-slip boundary condition leads to the enhancement of the heat transfer [Fig. 7(a)]. The Nusselt numbers have almost the same values for both types of boundary conditions [Figs. 7(b) and 7(c)] in the rotating case.

V. LINEAR INSTABILITY ANALYSIS

In this part, the stability of the basic flow is examined. Linear instability analysis is used to find a critical Rayleigh number, Ra_{Ec}, above which ($\text{Ra}_E > \text{Ra}_{Ec}$) the steady axisymmetric basic flow is always unstable. If $\text{Ra}_E < \text{Ra}_{Ec}$, then the basic flow is stable with respect to infinitesimal perturbation but may be unstable with respect to finite perturbation. To solve the eigenvalue problem, the linearized Navier-Stokes equation, the energy equation, and the Gauss equation are formulated. The most important property of the perturbation $\mathbf{u}$, Θ, $\tilde{\upsilon}$ for the velocity, temperature, and electric potential, respectively, is that due to the equatorial symmetry of the base flow, the perturbations satisfy either

$$\{u_r, u_\theta, u_\phi, \Theta, \tilde{\upsilon}\}(r, \theta, \phi)$$
$$= \{u_r, -u_\theta, u_\phi, \Theta, \tilde{\upsilon}\}(r, \pi - \theta, \phi), \tag{46}$$

which are equatorially symmetric (symmetry class I), or

$$\{u_r, u_\theta, u_\phi, \Theta, \tilde{\upsilon}\}(r, \theta, \phi)$$
$$= \{-u_r, u_\theta, -u_\phi, -\Theta, -\tilde{\upsilon}\}(r, \pi - \theta, \phi), \tag{47}$$

which are equatorially antisymmetric (symmetry class II). As we will see, unlike the case where the temperatures of the inner and outer enclosures are kept at constant values and only equatorially symmetric perturbations [Eq. (46)] are responsible for the instability [20], *both* classes are important in the problem considered. Hence, a rich variety of supercritical states is expected. According to linear instability theory, the basic flow $\mathbf{U}_0(r, \theta)$, the base temperature $T_0(r, \theta)$, and the base electric field $\mathbf{E}_{\text{base}} = -\nabla\upsilon_0(r) - \nabla\upsilon_1(r, \theta)$ are subjected to all possible infinitesimally small perturbations $\mathbf{u}(t, r, \theta, \phi)$ for the velocity, $\Theta(t, r, \theta, \phi)$ for the temperature, $\tilde{p}(t, r, \theta, \phi)$

for the pressure, and $\tilde{\upsilon}(t, r, \theta, \phi)$ for the electric potential. The linearized Navier-Stokes equation, energy equation, and Gauss equation to be solved are

$$\text{Pr}^{-1}\left[\frac{\partial\mathbf{u}}{\partial t} + (\mathbf{u}\nabla)\mathbf{U}_0 + (\mathbf{U}_0\nabla)\mathbf{u}\right]$$
$$= -\text{Pr}^{-1}\nabla\tilde{p} + \nabla^2\mathbf{u} - \frac{1}{4}\text{Ra}_E \cdot \Theta \cdot \nabla[\nabla\upsilon_0(r) + \nabla\upsilon_1(r, \theta)]^2$$
$$- \frac{1}{2}\text{Ra}_E \cdot T_0\nabla\{[\nabla\upsilon_0(r) + \nabla\upsilon_1(r, \theta)] \cdot \nabla\tilde{\upsilon}(r, \theta, \phi)\}$$
$$- \sqrt{\text{Ta}}\mathbf{e}_z \times \mathbf{u} + A \cdot \Theta r \sin\theta\mathbf{s}, \tag{48}$$

$$\frac{\partial\Theta}{\partial t} + (\mathbf{U}_0 \cdot \nabla)\Theta + (\mathbf{u} \cdot \nabla)T_0(r, \theta)$$
$$= \nabla^2\Theta + 2\frac{\text{Ra}_E}{\text{Ra}_T}[\nabla\upsilon_0(r) + \nabla\upsilon_1(r, \theta)] \cdot \nabla\tilde{\upsilon}(r, \theta, \phi), \tag{49}$$

$$\Delta\tilde{\upsilon} = \frac{B}{1 - B \cdot T_0(r, \theta)}(\Theta\Delta\upsilon_1(r, \theta)$$
$$+ \nabla T_0(r, \theta) \cdot \nabla\tilde{\upsilon}(r, \theta, \phi)$$
$$+ \nabla\Theta \cdot [\nabla\upsilon_0(r) + \nabla\upsilon_1(r, \theta)]. \tag{50}$$

Together with the continuity equation

$$\nabla \cdot \mathbf{u} = 0, \tag{51}$$

we obtain the system of equations that can be solved numerically. The boundary conditions for the perturbation are the same as in Eqs. (14) and (15). The boundary conditions for the temperature and the potential $\tilde{\upsilon}(r, \theta, \phi)$ are

$$\Theta = 0, \quad \tilde{\upsilon} = 0. \tag{52}$$

on the two surfaces. Due to the linearity of the stability equations and because the basic flow is steady, the temporal structure of the solution takes the form $\sim e^{\lambda t}$, where λ is the complex time growth rate. Moreover, the stability equations can be formulated *separately* for each azimuthal wave number m due to the orthogonality conditions of the spherical harmonics. The goal of the instability analysis is to find, for all relevant modes m, such Rayleigh numbers $\text{Ra}_E(m, \text{Ta})$ for fixed Taylor numbers for which the real part of λ is zero: $\text{Re}(\lambda) = 0$. Therefore, the smallest value of $\text{Ra}_E(m, \text{Ta})$ for each symmetry class of perturbations is the critical Rayleigh number,

$$\text{Ra}_{Ec}(\text{class I, class II}) = \min_m \text{Ra}_E(m, \text{Ta}), \tag{53}$$

and the azimuthal wave number m_c, which minimizes the Rayleigh number, is the critical azimuthal wave number. The imaginary part of the eigenvalue determines the kind of bifurcation. If $\text{Im}(\lambda) = 0$, then the flow becomes unstable with respect to the stationary perturbation. The instability sets in as an oscillated bifurcation when $\omega_c = \text{Im}(\lambda) > 0$, where ω_c is the circular oscillation frequency of the dominant perturbation with $m = m_c$. The value ω_c/m_c shows direction and drift velocity of the dominant perturbation. Although it is impossible to find the amplitude of the perturbed flow due to the *linear* theory, we can derive not only the critical parameters like Ra_{Ec} and m_c but also localization of the instability. Hence, linear instability analysis gives much information about three-

dimensional flow without performing expensive calculations of the three-dimensional flows.

The eigenvalue problem was solved by direct numerical integration. It is important to note that the instability problem must be solved for both types of perturbations [Eqs. (46) and (47)], i.e.,

$$\text{Ra}_{Ec} = \min \text{Ra}_{Ec}(\text{class I, class II}). \tag{54}$$

The same poloidal-toroidal decomposition is used for the velocity field as for the calculation of the base flow. In addition, however, azimuthal dependence was also considered to account for the general shape of the perturbation.

Linear instability analysis was performed for radii ratios $\eta = 0.7$ and $\eta = 0.8$ and for two types of boundary conditions. The stability curve has a closed form for all cases considered, i.e., the range in which the flow is stable to infinitesimal perturbations, bounded by the intervals $(0, \text{Ta}_c)$, $(0, \text{Ra}_{Ec})$, and the stability curve, where the numbers Ta_c and Ra_{Ec} depend on the radii ratio η and the type of boundary condition. In the first interval, only centrifugal and convective effects are responsible for the instability due to the atmospheric boundary conditions for the temperature, while buoyancy-induced instability predominates in the second interval. Moreover, near the equator, the buoyancy force and centrifugal force compete. Therefore, studying a situation in which these two effects occur is of particular interest for understanding atmospheric flows with a relatively simple model. We plot the critical Rayleigh number as a function of the Taylor number $\text{Ra}_{Ec}(\text{Ta})$ using the linear-log plot and the drift velocity of the dominant perturbation $\omega_{\text{drift}} = \omega_c/m_c$ vs. the Taylor number for each η due to the log-log representation. The subplots $\text{Ra}_{Ec}(\text{Ta})$ for small Taylor numbers are shown using the linear plot in both directions. The critical azimuthal wave numbers, m_c, are shown near the stability curves. The subscripts s and a indicate that the basic flow becomes unstable with respect to equatorially *symmetric* or equatorially *antisymmetric* perturbations, respectively.

The general property of the stability diagrams is that for large Taylor numbers the basic flow abruptly becomes unstable with respect to the perturbations at a low azimuthal wave number $m_c = 1$ and $m_c = 2$. Furthermore, in this case, the instability is located near the poles. Therefore, the critical Rayleigh numbers corresponding to the two symmetry classes are very close to each other. Nevertheless, the radii ratio and in particular the boundary conditions have a significant influence on the stability. Hence, it is necessary to consider the results of the instability analysis in detail.

A. Instability analysis for two rigid boundaries

In this section, we discuss the instability analysis for radii ratios $\eta = 0.7$ (Figs. 8 and 9) and $\eta = 0.8$ (Fig. 10).

According to the numerical calculations performed for $\eta = 0.7$, the axisymmetric steady basic flow loses its stability with respect to the axisymmetric oscillating perturbations in the nonrotating and slowly rotating case ($0 \leqslant \text{Ta} \leqslant 100$). The critical Rayleigh number ranges between $\text{Ra}_{Ec} = 2.26 \times 10^5$ and $\text{Ra}_{Ec} = 229\,250$. Further investigation of the axisymmetric oscillating flow can be performed, e.g., by means of the Floquet theory, but it is out of scope of the study presented. If
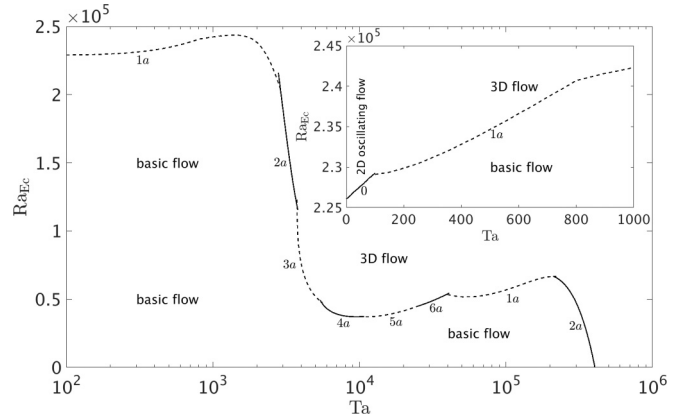

FIG. 8. Critical Rayleigh numbers vs. Taylor number for $\eta = 0.7$ and BC I. The numbers in the vicinity of the stability curves are the critical azimuthal wave numbers m_c.

the Taylor number increases ($100 \leqslant \text{Ta} \leqslant 3800$), then the basic flow becomes unstable with respect to perturbations with low azimuthal wave numbers $m_c = 1a$ and $m_c = 2a$. Both instabilities locate in the vicinity of the poles. The instability shifts toward the equator if the Taylor number increases from $\text{Ta} = 3800$ to $\text{Ta} = 4.0 \times 10^4$. The basic flow becomes unstable to the antisymmetric perturbations with $m_c = 3a - 6a$, as shown in Fig. 8. This part of the stability diagram is most interesting from the physical point of view because the Regime II, which good correlates with the atmosphere-like flows, belongs to this Taylor-number interval. According to linear instability theory the basic flow is unstable above the curve and the flow becomes three-dimensional structure and remains its stability with respect to the small perturbations below this curve. Further increasing in Taylor number ($4.0 \times 10^4 \leqslant \text{Ta} \leqslant 4.04 \times 10^5$) leads to the movement of the instability back to the poles. Hence, the range in which the flow is stable to infinitesimal perturbations, bounded by the intervals $(0, \text{Ta}_c = 4.04 \times 10^5)$, $(0, \text{Ra}_{Ec} = 2.26 \times 10^5)$ and the stability curve. In all cases considered, the instability sets in as an oscillating bifurcation. The perturbative flow drifts as shown in Figs. 9 with a velocity $\omega_{\text{drift}} = \omega_c/m_c$ in the rotating case, where ω_c is the frequency of the dominant
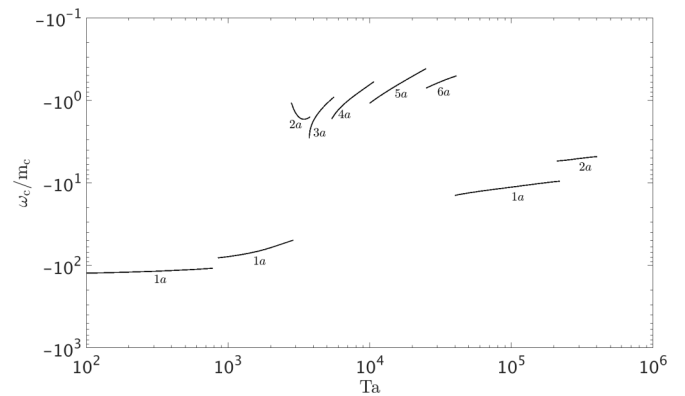

FIG. 9. Drift velocity vs. Taylor number for $\eta = 0.7$ and BC I. The numbers near the drift velocity curves are the critical azimuthal wave numbers m_c.
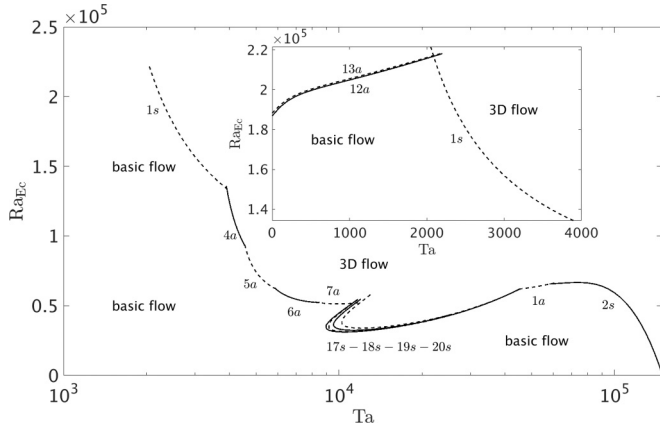
FIG. 10. Critical Rayleigh numbers vs. Taylor number for $\eta = 0.8$ and BC I. The numbers in the vicinity of the stability curves are the critical azimuthal wave numbers m_c.

perturbation. Note that the drift velocity is always negative, i.e., the perturbative flow moves in a retrograde direction.

It is worth to translate dimensionless parameters such as the critical Rayleigh number and the drift velocity of the dominant perturbation into the real physical values. We present the corresponding values in Table III with the radii ratio $\eta = 0.7$ as in the AtmoFlow experiment. Note that the absolute value of the drift velocity $\omega_{\text{drift}}^{\text{dim}}$ as opposed to the angular velocity Ω is only larger for small Taylor numbers Ta $= 10^2$. For medium and large Taylor numbers, the drift velocity of the perturbation becomes much lower.

Now let us consider the situation when the spherical gap becomes narrower, e.g., $\eta = 0.8$ (Fig. 10). In this case, the basic flow loses its stability with respect to the perturbations with $m_c > 0$ at Ta $= 0$. The dominant wave number is $m_c = 12$, but the critical Rayleigh numbers corresponding to the two classes, are so close (much less 1%) that it is impossible to say which class is responsible for the instability. This feature of the basic flow shows that the instability is located in the vicinity of the poles. Moreover, it is necessary to note that the Rayleigh numbers, $\text{Ra}_E(m = 13, \text{Ta})$, are larger than $\text{Ra}_{cE}(\text{Ta})$, but the difference is within 1%. This suggests that the supercritical three-dimensional flow has a very complex structure because of the nonlinear terms in the governing equations.

The next feature of the stability diagram at $\eta = 0.8$ is that both symmetry classes are responsible for the instability of the atmospherelike flows. Indeed, while the three-dimensional supercritical flow is antisymmetric with respect to equator with $m_c = 4a - 7a$ for $4 \times 10^3 \leqslant \text{Ta} \leqslant 11\,250$, the three-dimensional (3D) flow has a equatorially symmetric structure

when the Taylor number varies in the interval $8900 \leqslant \text{Ta} \leqslant 4.5 \times 10^4$ with $m_c = 17s - 20s$. Although in the narrow gap, the interval, which is relevant for atmospherelike flows, does not become essentially wider, it is much more interesting because our model under consideration enables rich variety of three-dimensional states and transitions. Indeed, due to the U-shaped trend of the stability curve it is possible, e.g., at Ta $= 10^4$ to obtain two different three-dimensional solutions, corresponding to both symmetry classes: with $m_c = 17s$ and $m_c = 7a$.

As in the case above, the basic flow becomes unstable with respect to perturbations with low azimuthal wave numbers for large Taylor numbers. Hence, the range, in which the flow is stable to infinitesimal perturbations, is bounded by the intervals $(0, \text{Ta}_c = 1.49 \times 10^5)$, $(0, \text{Ra}_{Ec} = 186\,880)$, and the stability curve. Behavior of the drift velocity is similar to the above considered case with $\eta = 0.7$ and is not presented here. The next important point is the discussion of the origin and location of instability. The azimuthally integrated kinetic energy of the nonaxisymmetric perturbation $e(r, \theta) = \int_0^{2\pi} \mathbf{u}^2 r \sin\theta \, d\phi$ is a useful tool for a study of this kind. This function of r and θ is shown in Fig. 11 along with the basic flow in the form of angular velocity (top row) and meridional circulation (second row) at the critical Rayleigh number. Moreover, it is preferable to discuss the origin of the instability in the case of $\eta = 0.8$, since it is the only spherical gap considered in which all types of instabilities occur. According to the instability analysis, the basic flow becomes unstable with respect to the low azimuthal wave numbers for small and large Taylor numbers. The instability is concentrated near the two poles, where the polar cells of the basic flow occur. Moreover, the transition is associated with the boundary layer because the instability is near the maximum of the radial [Fig. 11(a)] and longitudinal [Fig. 11(d)] velocity components of the basic flow. The flow in the other parts of the gap remains axisymmetrical. The instability between these cases is associated with equatorial cells. The basic flow becomes unstable with respect to the antisymmetric perturbations in the vicinity of the equator, as shown in Fig. 11(b). The instability is concentrated near the equator but not quite there and is associated with radial jet of the basic flow. The radial velocity component of the three-dimensional flow, shown in Fig. 12, has a wavy structure with $m = 6a$ periodicity in ϕ, in agreement with instability theory. As expected, most of the energy of the flow is concentrated near the equator. Further increasing the Taylor number leads to a different kind of instability. The basic flow is unstable to symmetrical perturbances [Fig. 11(c)]. The maximum kinetic energy of the perturbation is now exactly at the equator, and the instability is associated with the radial component of the meridional circulation. In agreement

TABLE III. Connection between nondimensional characteristics (Ra_{EcL}, ω_{drift}) of the instability and dimensional characteristics (V_{rms}, $\omega_{\text{drift}}^{\text{dim}}$) for $\eta = 0.7$ and BC I. m_c are the critical azimuthal wave numbers.

Ta	Ω (rad s^{-1})	Ra_{EcL}	$V_{\text{rms,crit}}$ (V)	m_c	$\lvert \omega_{\text{drift}} \rvert$	$\omega_{\text{drift}}^{\text{dim}}$ (rad s^{-1})
10^2	0.03588	229100	1710.74	$1a$	124.39	0.08558
10^4	0.3588	37146	688.85	$4a$	0.6482	0.4459×10^{-3}
10^5	1.1346	56796	851.79	$1a$	11.29	0.7769×10^{-2}

$Ta = 3 \cdot 10^3$
$Ra_{Ec} = 156940$
$m_c = 1s$

$Ta = 7 \cdot 10^3$
$Ra_{Ec} = 54590$
$m_c = 6a$

$Ta = 10^4$
$Ra_{Ec} = 31198$
$m_c = 17s$
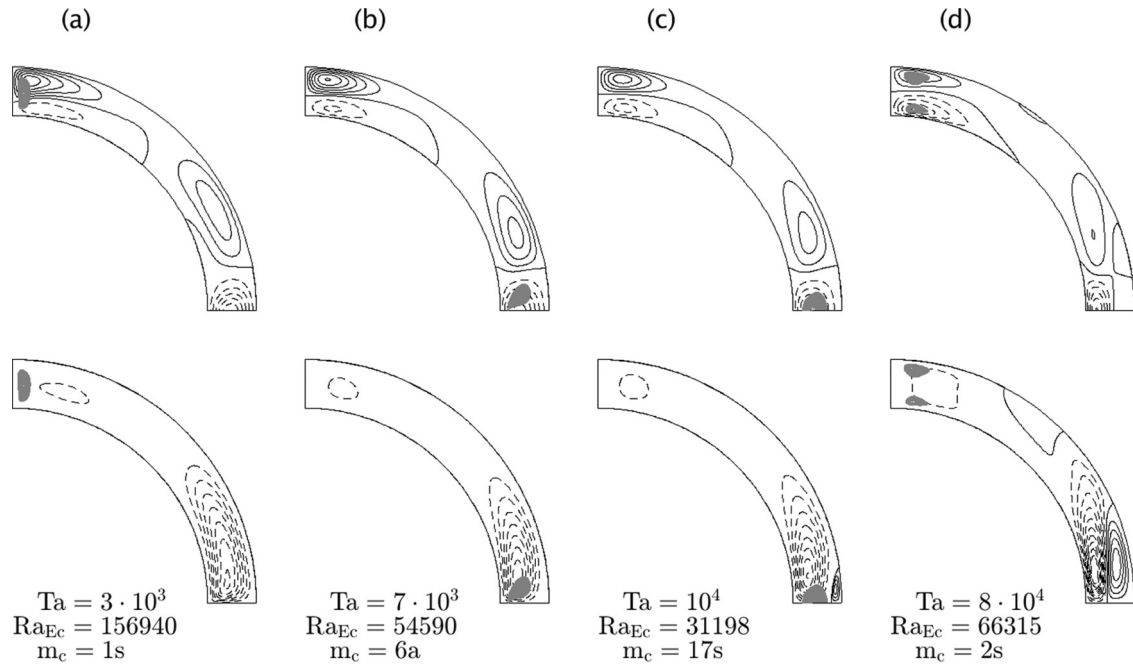
$Ta = 8 \cdot 10^4$
$Ra_{Ec} = 66315$
$m_c = 2s$

FIG. 11. Basic flow and the location of the instability for $\eta = 0.8$ and BC I. The top row shows the isolines of the azimuthal velocity of the basic flow with maximal and minimal values (a) $+10.0$ (2.0), -20.0 (4.0); (b) $+4.8$ (0.8), -10.0 (2.0); (c) $+2.0$ (0.5), -5.0 (1.0); and (d) $+1.2$ (0.4), -2.0 (0.4). The dotted (solid) lines indicate negative (positive) values of the azimuthal velocity. The second row shows the isolines of the meridional circulation of the basic flow with maximal and minimal values (a) -42.0 (6.0); (b) -14.0 (2.0); (c) $+0.07$ (0.01); -6.4 (0.8); and (d) $+0.8$ (0.2), -2.0 (0.2). The dotted (solid) lines indicate negative (positive) values of the stream function. The corresponding vortices rotate counterclockwise (clockwise). The contour intervals are shown in brackets. Gray indicates the azimuthally integrated kinetic energy of the nonaxisymmetric instability.

with the instability results, the three-dimensional flow has a periodicity of $m = 17s$ in ϕ for $Ta = 10^4$. The supercritical three-dimensional flow again has a steady wave structure. The same transition has been detected in the cylindrical annulus. The baroclinic origin of the instability can be seen particularly well in the equatorial plane in Fig. 13 for the temperature. The next three-dimensional solution is obtained for $Ta = 10^5$

(Fig. 14). The linear instability analysis predicts that the basic flow becomes unstable with respect to perturbations with low azimuthal wave number, $m = 2s$. Moreover, the perturbation locates in vicinity of the poles. Exactly this structure of the 3D flow we calculated at $Ta = 10^5$ and $Ra_E = 6.5 \times 10^4$: The supercritical flow remains its axisymmetrical structure but at the poles.
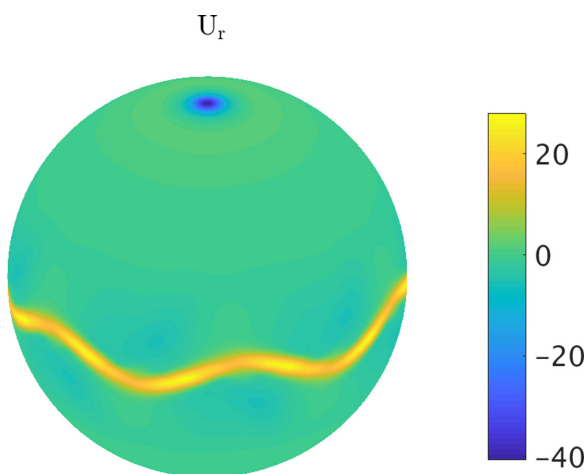

FIG. 12. Radial velocity component of the three-dimensional flow on the surface $r = 4.25$ for $\eta = 0.8$, $Ta = 7 \times 10^3$, and $Ra_E = 8 \times 10^4$.
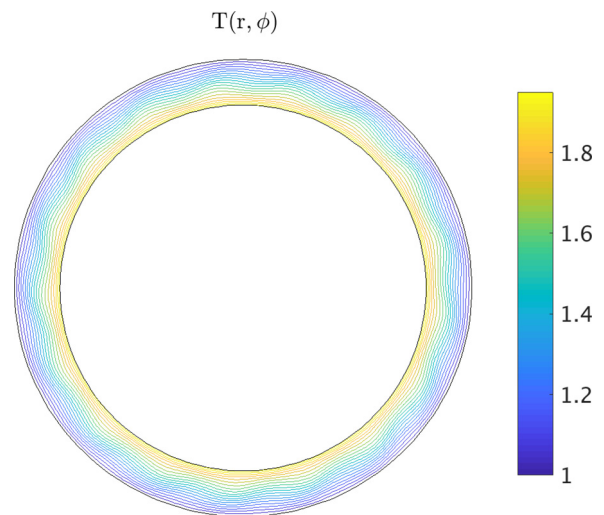

FIG. 13. Contours of the temperature at the equator plane for $\eta = 0.8$, $Ta = 10^4$, and $Ra_E = 31\,600$.
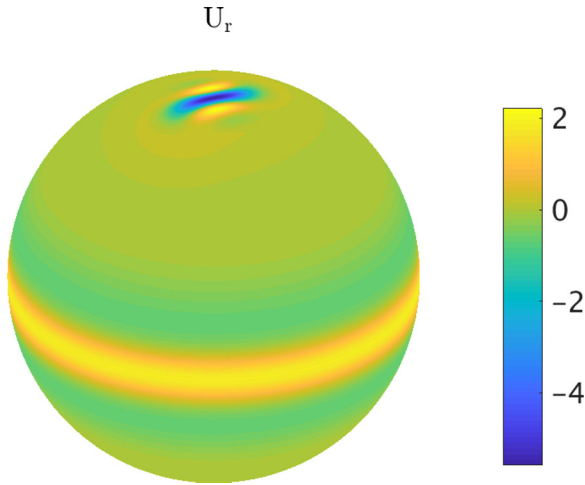
FIG. 14. Radial velocity component of the three-dimensional flow on the surface $r = 4.25$ for $\eta = 0.8$, $\mathrm{Ta} = 10^5$, and $\mathrm{Ra}_E = 6.5 \times 10^4$.

B. Instability analysis for inner rigid and outer free boundary

In this section, we discuss the instability analysis for radii ratios $\eta = 0.7$ (Figs. 15 and 16) and $\eta = 0.8$ (Fig. 17) in the case when free-slip boundary condition is valid on the outer surface.

Beginning with the radii ratio $\eta = 0.7$ (Fig. 15), we found that basic flow loses its stability to the axisymmetric oscillating perturbations solely in the nonrotating case. The critical Rayleigh number is $\mathrm{Ra}_{Ec} = 285\,200$. Further shape of the stability curve is very unexpected. The basic flow becomes unstable with respect to perturbations with dominant azimuthal wave number $m = 1a$ if the Taylor number varies between $\mathrm{Ta} \approx 0$ and $\mathrm{Ta} = 4100$. Only in small interval $\mathrm{Ta} \in [4100, 7800]$, symmetric perturbations with $m_c = 11s$ and $m_c = 12s$ are responsible for the instability. This region is essential for our study because all three cells exist here even for $\mathrm{Ra}_E < \mathrm{Ra}_{Ec}$ (Fig. 5, Regime II).

As in the case considered above, further increasing in Taylor number ($7800 \leqslant \mathrm{Ta} \leqslant 268\,334$) causes the instability

FIG. 16. Drift velocity vs. Taylor number for $\eta = 0.7$ and BC II. The numbers in the vicinity of the drift velocity curves are the critical azimuthal wave numbers m_c.

with low wave numbers. Hence, the range in which the basic flow remains stable bounded by the intervals $(0, \mathrm{Ta}_c = 268\,334)$, $(0, \mathrm{Ra}_{Ec} = 285\,200)$, and the stability curve. The shape of the drift velocity shown in Fig. 16. The instability drifts westwards, i.e., has a negative sign. Hence, we have a qualitatively similar situation as in the case with sloping endwalls considered in Refs. [7,8]. These studies observed a clockwise (retrograde) drift in the cylindrical annulus in the case when $\partial D/\partial r > 0$, where D is the fluid depth. Moreover, retrograde drift has been observed in the classical cylindrical gap in Ref. [5]. The absolute value of the drift velocity $\omega_{\mathrm{drift}}^{\mathrm{dim}}$ is significantly smaller than Ω for all Taylor numbers (Table IV).

As in the case when both surfaces are rigid, the basic flow becomes unstable with respect to high wave numbers if the radii ratio increases, as shown in (Fig. 17) for $\eta = 0.8$, i.e., in the interval $\mathrm{Ta} \in [0, 14]$ the three-dimensional flow promises to be chaotic. Critical Rayleigh number decreases from $\mathrm{Ra}_{Ec} = 218\,200$ at $\mathrm{Ta} = 14$ to $\mathrm{Ra}_{Ec} = 36\,870$ at $\mathrm{Ta} = 3000$, i.e., increasing in Taylor number destabilizes the basic flow as in all cases considered. The critical azimuthal wave numbers increase dramatically as the Taylor number varies between $\mathrm{Ta} = 3000$ and $\mathrm{Ta} = 54\,000$. This Taylor-number interval is of interest for our study. Unfortunately, the critical
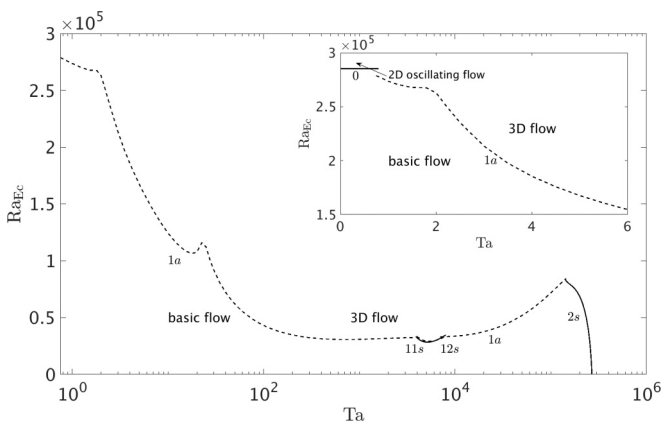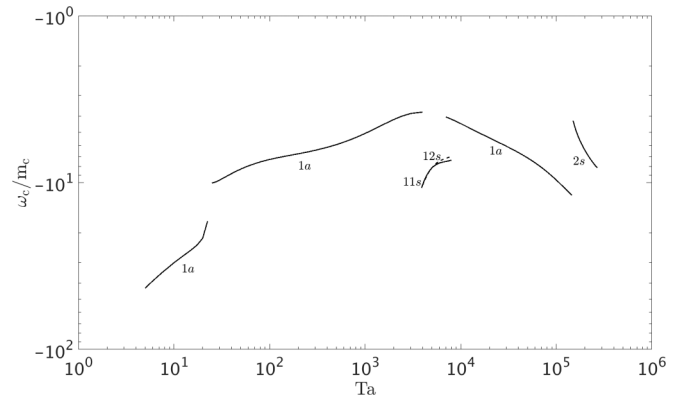

FIG. 15. Critical Rayleigh numbers vs. Taylor number for $\eta = 0.7$ and BC II. The numbers in the vicinity of the stability curves are the critical azimuthal wave numbers m_c.
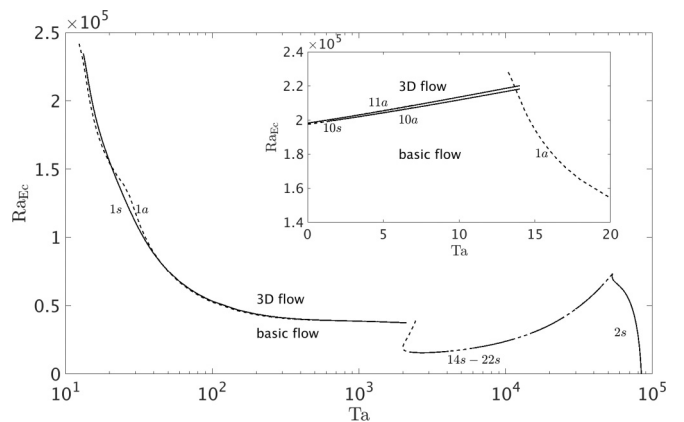

FIG. 17. Critical Rayleigh numbers vs. Taylor number for $\eta = 0.8$ and BC II. The numbers in the vicinity of the stability curves are the critical azimuthal wave numbers m_c.

TABLE IV. Connection between nondimensional characteristics (Ra_{EcL}, ω_{drift}) of the instability and dimensional characteristics (V_{rms}, ω_{drift}^{dim}) for $\eta = 0.7$ and BC II. m_c are the critical azimuthal wave numbers.

Ta	Ω (rad s^{-1})	Ra_{EcL}	$V_{rms,crit}$ (V)	m_c	$|\omega_{drift}|$	ω_{drift}^{dim} (rad s^{-1})
10^2	0.03588	43 098	742.0	1a	7.2702	0.005002
10^4	0.3588	33 638	655.52	1a	4.4269	0.003046
10^5	1.1346	71 750	957.38	1a	9.6486	0.005638

Rayleigh number is to small to trigger the Ferrel cell. The range in which the basic flow remains stable bounded by the intervals (0, Ta$_c$ = 84 143), (0, Ra$_{Ec}$ = 218 200), and the stability curve.

The location of the instability for different Taylor numbers is shown in Fig. 18 for $\eta = 0.8$. The instability is associated with the azimuthal flow for small Taylor numbers, as shown in Fig. 18(a). The increase in Taylor numbers causes a shift in the instability toward the outer surface [Fig. 18(b)] and is associated again with the azimuthal velocity component of the basic flow in the region of the polar cells. Note that both flows become unstable with respect to perturbations with $m_c = 1$. A further increase in the Taylor number causes the instability to occur at the equator with high m_c [Fig. 18(c)]. This type of instability has the same origin as in the case of two rigid bounding surfaces. Finally, the azimuthal flow of the basic flow is responsible for the instability at large Taylor numbers [Fig. 18(d)]. Regimes Figs. 18(a)–18(c) are perspective for our study. Unfortunately, regime Fig. 18(d) is too far from the atmospherelike model and cannot be considered.

C. Influence of the induced field

The next issue to be examined is the role played by the induced electric field $\tilde{\mathbf{E}} = -\nabla \tilde{v}$. This field occurs not only because an imposed electric field influences the flow but also because the flow varies the electric field. To clarify their influence, we have performed some calculations of the critical Rayleigh numbers both considering the Gauss equation Eq. (50) and corresponding terms in the Navier-Stokes and energy equations and without taking into account the induced field. The results for two rigid bounding surfaces are presented in Table V. In all cases, the induced field has stabilizing effect, i.e., the critical Rayleigh numbers become larger if the induced field is involved in the numerical model. The induced electric field is particularly important, when the Rayleigh number is large and the Taylor number is small.

In contrast to the case when both surfaces are rigid, the induced electric field is not significant when the outer surface is free, i.e., the corresponding critical Rayleigh numbers change within 0.4–1.42% (Table VI).

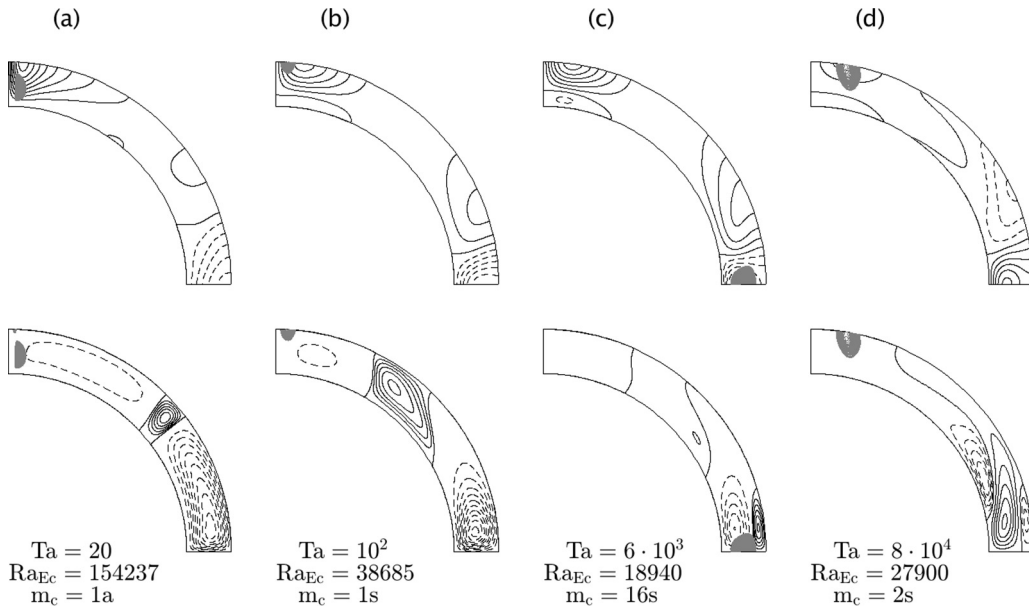| (a)	(b)	(c)	(d)
Ta = 20	Ta = 10^2	Ta = $6 \cdot 10^3$	Ta = $8 \cdot 10^4$
Ra$_{Ec}$ = 154237	Ra$_{Ec}$ = 38685	Ra$_{Ec}$ = 18940	Ra$_{Ec}$ = 27900
m$_c$ = 1a	m$_c$ = 1s	m$_c$ = 16s	m$_c$ = 2s

FIG. 18. Basic flow and the location of the instability for $\eta = 0.8$ and BC II. The top row shows isolines of the azimuthal velocity of the basic flow with maximal and minimal values (a) $+24.0$ (3.0), -5.0 (1.0); (b) $+10.0$ (2.0), -10.0 (2.0); (c) $+2.4$ (0.4), -2.0 (0.4); and (d) $+1.0$ (0.2), -0.6 (0.2). The dotted (solid) lines indicate a negative (positive) value of the angular velocity. The second row shows isolines of the meridional circulation of the basic flow with maximal and minimal values (a) $+5.0$ (1.0), -80.0 (10.0); (b) $+0.25$ (0.05), -25.0 (2.5); (c) $+0.45$ (0.09), -4.0 (0.8); and (d) $+0.45$ (0.09), -0.12 (0.03). The dotted (solid) lines indicate negative (positive) values of the stream function. The corresponding vortices rotate counterclockwise (clockwise). The contour intervals are shown in brackets. Gray shows the azimuthally integrated kinetic energy of the nonaxisymmetric instability.

TABLE V. Influence of the induced electric field on the critical Rayleigh number (BC I).

Ta	$\eta = 0.7$ $\overline{\mathrm{Ra}_{cE}}$	$\mathrm{Ra}_{cE}^{\text{no induction}}$	Diff. (%)	Ta	$\eta = 0.8$ $\overline{\mathrm{Ra}_{cE}}$	$\mathrm{Ra}_{cE}^{\text{no induction}}$	Diff. (%)
3×10^3	189 976	168 303	12.88	3×10^3	156 939	151 935	3.29
2×10^4	41 484	40 697	1.93	2×10^4	38 127	37 765	0.95
10^5	56 796	56 450	0.61	10^5	59 265	58 470	1.36

TABLE VI. Influence of the induced electric field on the critical Rayleigh number (BC II).

Ta	$\eta = 0.7$ $\overline{\mathrm{Ra}_{cE}}$	$\mathrm{Ra}_{cE}^{\text{no induction}}$	Diff. (%)	Ta	$\eta = 0.8$ $\overline{\mathrm{Ra}_{cE}}$	$\mathrm{Ra}_{cE}^{\text{no induction}}$	Diff. (%)
50	61 881	61 630	0.41	50	75 202	76 266	1.42
5000	28 393	28 106	1.02	5000	17 700	17 569	0.75
2×10^5	68 697	68 423	0.40	2×10^5	53 327	52 693	1.20

TABLE VII. Influence of the centrifugal force on the critical Rayleigh number (BC I).

Ta	$\eta = 0.7$ $\overline{\mathrm{Ra}_{cE}}$	m_c	$\mathrm{Ra}_{cE}^{\text{without c.f.}}$	m_c	Diff. (%)	Ta	$\eta = 0.8$ $\overline{\mathrm{Ra}_{cE}}$	m_c	$\mathrm{Ra}_{cE}^{\text{without c.f}}$	m_c	Diff. (%)
10^4	37 146	4a	37 725	4a	1.56	10^4	31 198	17s	24 029	17s	−22.9
10^5	56 796	1a	77 661	5a	36.7	10^5	59 265	2s	45 693	21s	−22.9

TABLE VIII. Influence of the centrifugal force on the critical Rayleigh number (BC II).

Ta	$\eta = 0.7$ $\overline{\mathrm{Ra}_{cE}}$	m_c	$\mathrm{Ra}_{cE}^{\text{without c.f.}}$	m_c	Diff.(%)	Ta	$\eta = 0.8$ $\overline{\mathrm{Ra}_{cE}}$	m_c	$\mathrm{Ra}_{cE}^{\text{without c.f}}$	m_c	Diff.(%)
10^4	33 638	1a	33 920	13s	0.84	10^4	23 907	17s	17 413	17s	−27.16
5×10^4	51 846	1a	62 873	1a	21.27	5×10^4	69 628	22s	34 933	22s	−49.83

D. Influence of the centrifugal force

We complete this section with a discussion of the influence on the centrifugal force. Even in the cylindrical geometry, this force must be incorporated into the equations because the temperature cannot be represented as a gradient of the scalar function that can be combined with pressure at sufficiently high Rayleigh numbers [6,32]. Centrifugal effects are much more important in the spherical geometry, particularly with atmospherelike boundary conditions for the temperature. We performed some calculations of the critical Rayleigh numbers with and without centrifugal force for both kinds of boundary conditions. The results, summarized in Table VII (BC I) and Table VIII (BC II), show that the centrifugal force essentially influences not only the critical Rayleigh number but also the structure of three-dimensional flow for *both* kinds of the boundary conditions.

VI. SUMMARY AND CONCLUSIONS

The goal of the study presented here was to perform the numerical analysis of the convective flow in the rotating spherical gap caused by the atmospherelike boundary conditions for the temperature field. These boundary conditions reflect the most important features of the temperature on the Earth's surface due to the Sun's radiation. Two kinds of boundary conditions for the velocity field have been taken into account: While the first case corresponds to a situation when both bounding surfaces are rigid, the second one corresponds to the inner rigid and outer free bounding surface. The radial force field was produced due to the dielectrophoretic effect.

The basic flow is steady axisymmetric and equatorially symmetric. We found three regimes for $\eta = 0.7$. These regimes occur as a result of competition between the buoyancy force, Coriolis force and centrifugal force. The meridional circulation, corresponding to the second regime, is most interesting from the physical point of view because this one produces atmospherelike flows of a qualitatively correct shape, consisting in polar and equatorial or Hadley vortices. The fourth regime has been observed when the gap becomes narrower at $\eta = 0.8$. In contrast to Regime II, the small-scale clockwise rotating vortex, associated with the Ferrel or midlatitude cell, occurs between large-scale counterclockwise rotating vortices. This regime feeds energy from the polar and Hadley cells in good agreement with the three-cellular atmospheric model. Although our a quite simple model (rotation + polar dependent temperature conditions) shows many similarities with atmospheric flows, it is worth to mention reasons of deviations from them. (1) The realistic gap ($\eta = 0.997$) is much narrower in contrast to the considered. (2) Not only the Coriolis force but also temperature dependent [due to density $\rho(T)$] centrifugal force must be taken into account. (3) The Prandtl number is $\mathrm{Pr} = 10.43$ corresponds to Novec7200. This Pr is much larger than of the air with $\mathrm{Pr} = 0.71$. Unfortunately, we need the silicon oil as working fluid for producing the radial force field using the dielectrophoretic effect. (4) The value of $\Delta T = 7.5$ K is much smaller in comparison to the temperature gradient between equator and pole. Our choice is limited by the validity of the Boussinesq approach. Anyway, the variety of the regimes is

closely connected with polar-angle-dependent thermal boundary conditions, which is key for understanding and simulating atmospheric flows of this kind. Only Regime I was observed when both spherical surfaces are maintained at constant temperatures ($T_{\mathrm{in}} > T_{\mathrm{out}}$) [20].

The stability of the basic flow has been studied in frames of the linear instability analysis. The results were presented in the form of diagrams $\mathrm{Ra}_{Ec}(\mathrm{Ta})$, i.e., critical Rayleigh numbers were calculated as a function of the Taylor number for a fixed radii ratio and Prandtl number. The analysis reveals that the basic flows lose their stability with respect to either antisymmetric perturbations (for $\eta = 0.7$) or symmetric perturbations for $\eta = 0.8$ with respect to the equator. This is a very surprising behavior of the instability, particularly taking into account that only symmetric perturbations are dominant when both surfaces are maintained at a constant temperature. The next unexpected result of the linear instability analysis is the closed form of the stability diagrams. In other words, if the buoyancy force is absent, then the critical Taylor number exists above which the flow becomes unstable with respect to low azimuthal wave numbers. However, in the nonrotating case and at very small Taylor numbers, if the Rayleigh number exceeds a critical value, then the basic flow either becomes a two-dimensional oscillating structure ($\eta = 0.7$) or undergoes a transition into a three-dimensional chaotic state ($\eta = 0.8$). Again, these results differ completely from the behavior of the stability curve when the temperatures of the bounding surfaces are constant. If the dielectric heating is negligible [16], then the critical Rayleigh number changes according to $\mathrm{Ra}_{Ec} \sim \mathrm{Ta}^{2/3}$. This dependence was also theoretically found by Roberts [33] in the cylindrical geometry. When the dielectrical heating is taken into account [20], this dependence is stronger, $\mathrm{Ra}_{Ec} \sim \mathrm{Ta}$. Hence, from the basic flow analysis and shape of the stability curves we can conclude that the "classical" spherical annulus model with constant temperatures on the both surfaces cannot be used to simulate of the atmospherelike flows.

Based on the results presented, a number of experiments and further numerical investigations can be suggested. (1) According to the stability analysis, the drift velocity and the rotation rate have opposite signs for a wide range of Taylor numbers. This effect could be investigated numerically in detail. The next issue is the analytical connection between the drift rates and Ω. According to the theoretical prediction [34] this connection $\omega_{\mathrm{drift}} = \omega_c/m_c \propto \Omega^{-\zeta}$ with $\zeta = 1$. This power law has been observed experimentally in the baroclinic annulus with $\zeta = 1.17$ [10,35]. The first results in the spherical geometry show that the power law is valid but with higher value of ζ, e.g., $\zeta = 2$ for the dominant wave number $m_c = 5$ presented in Fig. 9. (2) Since the critical wave numbers m_c corresponding to the symmetric mode increase drastically with increasing in η, the supercritical three-dimensional flows are expected to have a quite complex structure. Research of that topic could answer many open questions concerning the kind of bifurcations occurring, the amplitude of the perturbation, the heat transfer of the supercritical states and the transition into the further states. The following scenarios and transitions can be realized: Regime 2 $\rightarrow$ steady wave $\rightarrow$ amplitude vacillation $\rightarrow$ irregular flow for fixed Taylor number and increasing Rayleigh number; Regime 3 $\rightarrow$ steady

wave → amplitude vacillation → irregular flow for fixed Rayleigh number and increasing Taylor number analogically to the corresponding simulations in the cylindrical annulus [6]. (3) The next important issue is the influence of the ΔT. Only a lower symmetric regime is observed when ΔT is small ($\Delta T = 1$ K) in the cylindrical annulus. The upper symmetric regime appears when ΔT increases (3 K $\leqslant \Delta T \leqslant$ 30 K) [2,6]. Therefore, it is important to clarify whether the Regime 3 occurs at small ΔT and how the temperature gradient influences the stability. (4) The radii ratio η seems to be a very important parameter and may be the most essential. Initial results show that the three-cell atmospheric model can be realized better if the spherical gap becomes narrower. Therefore, it is worth performing a similar investigations for $\eta = 0.85$ and $\eta = 0.9$.

APPENDIX: DERIVATION OF THE EQUATION FOR THE CONDUCTIVE STATE

The solution of the equation corresponding to the conductive state

$$\Delta T_{\text{cond}}(r, \theta) = 0 \tag{A1}$$

with boundary conditions Eqs. (27) and (28) can be written in the following form:

$$T_{\text{cond}}(r, \theta) = T_{\text{rad}}(r) + \sum_{\ell=1}^{\infty} (C_{1\ell} r^{\ell} + C_{2\ell} r^{-\ell-1}) P_{\ell}(\cos \theta), \tag{A2}$$

where

$$T_{\text{rad}}(r) = \left[-\frac{\eta}{1-\eta} + \frac{\eta}{(1-\eta)^2} \frac{1}{r} \right] D_{10},$$
$$+ \left[\frac{1}{1-\eta} - \frac{\eta}{(1-\eta)^2} \frac{1}{r} \right] D_{20}, \tag{A3}$$

$$D_{10} = \frac{1}{2} \int_0^{\pi} T_{\text{in}}(\theta) \sin \theta \, d\theta$$

$$D_{20} = \frac{1}{2} \int_0^{\pi} T_{\text{out}}(\theta) \sin \theta \, d\theta, \tag{A4}$$

$$C_{1\ell} = -\frac{(1-\eta)^{\ell}}{(1-\eta^{2\ell+1})} (\eta^{\ell+1} D_{1\ell} - D_{2\ell}),$$

$$C_{2\ell} = \frac{\eta^{\ell+1}}{(1-\eta)^{\ell+1}(1-\eta^{2\ell+1})} (D_{1\ell} - \eta^{\ell} D_{2\ell}), \tag{A5}$$

$$D_{1\ell} = \frac{2\ell+1}{2} \int_0^{\pi} T_{\text{in}}(\theta) P_{\ell}(\cos \theta) \sin \theta \, d\theta,$$

$$D_{2\ell} = \frac{2\ell+1}{2} \int_0^{\pi} T_{\text{out}}(\theta) P_{\ell}(\cos \theta) \sin \theta \, d\theta \tag{A6}$$

for $\ell = 1$, etc. Substituting of the expression from Eq. (A2) into Eqs. (41) yields

$$Q_{\text{in}}^{\text{cond}} = Q_{\text{out}}^{\text{cond}} = -\frac{4\pi \eta}{(1-\eta)^2} (-D_{10} + D_{20}). \tag{A7}$$

Because $D_{10} = 1.1244$, $D_{20} = \frac{\sinh(a_{\text{th}}) - a_{\text{th}} \cosh(a_{\text{th}})}{a_{\text{th}}[1 - \cosh(a_{\text{th}})]} = 0.98$, we have

$$Q_{\text{in}}^{\text{cond}} = Q_{\text{out}}^{\text{cond}} = 0.1444 \frac{4\pi \eta}{(1-\eta)^2}. \tag{A8}$$

[1] R. Hide, Philos. Trans. R. Soc. Lond. A Math. Phys. Eng. Sci. **250**, 441 (1958).

[2] W. Fowlis and R. Hide, J. Atmos. Sci. **22**, 541 (1965).

[3] R. Hide, P. Mason, and R. Plumb, J Atmos. Sci. **34**, 930 (1977).

[4] P. Read, J. Fluid Mech. **168**, 255 (1986).

[5] G. Williams, J. Fluid Mech. **49**, 417 (1971).

[6] A. Randriamampianina, W.-H. Fruh, and P. M. P. L. Read, J. Fluid Mech. **561**, 359 (2006).

[7] M. Bastin and P. Read, J. Fluid Mech. **339**, 173 (1997).

[8] M. Bastin and P. Read, Phys. Fluids **10**, 375 (1998).

[9] M. Vincze, U. Harlander, T. von Larcher, and C. Egbers, Nonlin. Process. Geophys. **21**, 237 (2014).

[10] M. Vincze, S. Borchert, U. Achatz, T. von Larcher, M. Baumann, C. Liersch, S. Remmler, T. Beck, K. Alexandrov, C. Egbers, J. Froehlich, V. Heuveline, S. Hickel, and U. Harlander, Meteorol. Z. **23**, 611 (2015).

[11] H. Scolan and P. Read, Exp. Fluids **58**, 75 (2017).

[12] S. Wright, S. Su, H. Scolan, R. Young, and P. Read, Fluids **2**, 41 (2017).

[13] R. Hollerbach, Int. J. Numer. Methods Fluids **732**, 773 (2000).

[14] F. Zaussinger, P. Canfield, A. Froitzheim, V. Travnikov, P. Haun, M. Maier, A. Meyer, P. Heintzmann, T. Driebe, and C. Egbers, Microgfav. Sci. Tech. **31**, 569 (2019).

[15] C. Egbers, W. Beyer, A. Bonhage, R. Hollerbach, and P. Beltrame, Adv. Space Res. **32**, 171 (2003).

[16] V. Travnikov, C. Egbers, and R. Hollerbach, Adv. Space Res. **32**, 181 (2003).

[17] B. Futterer, C. Egbers, N. Dahley, S. Koch, and L. Jehring, Acta Astronaut. **66**, 193 (2010).

[18] B. Futterer, N. Dahley, S. Koch, N. Scurtu, and C. Egbers, Acta Astronaut. **71**, 11 (2012).

[19] B. Futterer, A. Krebs, A.-C. Plesa, F. Zaussinger, R. Hollerbach, D. Breuer, and C. Egbers, J. Fluid Mech. **735**, 647 (2013).

[20] V. Travnikov, F. Zaussinger, P. Haun, and C. Egbers, Phys. Rev. E **101**, 053106 (2020).

[21] L. Landau and E. M. Lifshitz, *Electrodynamics of Continuos Media, Course of Theoretical Physics*, Vol. 8, 2nd ed. (Elsevier Butterworth-Heinemann, Burlington, MA, 1984).

[22] R. J. Turnbull and J. R. Melcher, Phys Fluids **12**, 1160 (1969).

[23] J. Melcher, *Continuum Electromechanics* (MIT Press, Cambridge, MA, 1981).

[24] P. Roberts, Q. J. Mech. Appl. Methods **22**, 211 (1969).

[25] H. Yoshikawa, O. Crumeyrolle, and I. Mutabazi, Phys. Fluids **25**, 024106 (2013).

[26] H. N. Yoshikawa, M. Tadie Fogaing, O. Crumeyrolle, and I. Mutabazi, Phys. Rev. E **87**, 043003 (2013).

[27] I. Yavorskaya, N. Fomina, and Y. Belyaev, Acta Astronaut. **11**, 179 (1984).

[28] F. Feudel, K. Bergemann, L. S. Tuckerman, C. Egbers, B. Futterer, M. Gellert, and R. Hollerbach, Phys. Rev. E **83**, 046304 (2011).

[29] I. Mutabazi, H. Yoshikawa, M. Fogaing, V. Travnikov, O. Crumeyrolle, B. Futterer, and C. Egbers, Fluid Dyn. Res. **48**, 061413 (2016).

[30] B. L. Smorodin, Tech. Phys. Lett. **27**, 1062 (2001).

[31] B. L. Smorodin and V. G. Velarde, J. Electrostat. **50**, 205 (2001).

[32] A. Randriamampianina, E. Leonardi, and P. Bontoux, in *Advances in Computational Heat Transfer*, edited by G. De Vahl Davis and E. Leonardi (Begell House, Danbury, CT, 1998), pp. 322–329.

[33] P. Roberts, Philos. Trans. R. Soc. A **263**, 1136 (1968).

[34] E. Eady, Tellus **1**, 33 (1949).

[35] J. Fein, Geophys. Astrophys. Fluid Dyn. **5**, 213 (1973).